Neutrino-Oxygen Neutral Current Quasi-Elastic measurement in the water Cherenkov detector

March, 2019

Daisuke Fukuda

Graduate School of
Natural Science and Technology
(Doctor's Course)

OKAYAMA UNIVERSITY

Abstract

Super-Kamiokande(SK) is a large water Cherenkov detector aimed at the discovery of proton decay and the detection of neutrinos. The T2K(Tokai-to-Kamioka) experiment is a long-baseline neutrino experiment with the SK as a far-detector. The main topic of this thesis is the measurement of neutrino-oxygen Neutral Current Quasi-Elastic(NCQE) interactions.

The main purpose of measuring NCQE interactions is to reduce the background in the supernova relic neutrino (SRN) search in the SK-Gd experiment, in which gadolinium(Gd) is dissolved in pure water in the SK tank. Because the NCQE interaction of an atmospheric neutrino often produces a signal similar to that of an SRN, it serves as the main contributor to the background in the SRN search. Thus, understanding the NCQE reaction is necessary for the successful observation of SRNs.

The NCQE interaction of neutrinos in the SK can be observed through the reaction with an oxygen nucleus in water. When this reaction occurs, a nucleon is knocked out of the oxygen nucleus. At this time, the oxygen nucleus becomes an excited nucleus and often releases a de-excitation gamma ray of approximately 6 MeV, which can be observed in the SK.

In this paper, NCQE interactions from the T2K experimental data from January 2010 to May 2013 were analyzed, and 102 NCQE events were observed. The NCQE cross-section was measured at 2.01×10^{-38} cm^2 $\pm$ 0.27(stat.) $\pm \, ^{0.69}_{0.39}$(sys.). The second topics of this paper concerns the observation of neutrons released by an NCQE interaction. Neutrons released in water are eventually captured by a hydrogen nucleus and emit a 2.2 MeV gamma-ray. In this thesis, the observation of 2.2 MeV gamma-rays was achieved by multivariate analysis using a neural network. A total of 32 neutrons were observed in 102 NCQE events with a 24.3% detection efficiency, and the number of background events was estimated to be 2.04. Considering the detection efficiency, an averaged of 1.21 $\pm$ 0.25 neutrons are emitted in a single NCQE event. However, the simulation in this work estimates 1.77 neutrons. This result suggests that the number of emitted neutrons via NCQE is greater in the simulation than in the actual data.

Acknowledgments

I would like to express my gratitude in here to all the people who help me.

First and foremost, Professor Yusuke Koshio, I would like to thank you for giving me the opportunity of research and good advice. I could continue my research as he is my supervisor. Especially, he also understood my character and mind and spent a very enormous amount of time on me. This thesis would never exist without his support. Thank you from the bottom of my heart.

I would like to thank you all for giving me a lot of advice on my study. They taught analysis technique and problem to me. Special thanks go to Akira Konaka, Hirohisa Tanaka, Tsuyoshi Nakaya, Masato Shiozawa, Yoshinari Hayato, Shouei Nakayama, Yasuhiro Nishimura, Roger Wendel, Marek Ankowski, Yasuhiro Nakajima, Takatomi Yano, Makoto Sakuda, Kunxian Huang, Yuki Nakano, Seiko Hirota, Yusuke Suda, Yuji Okajima, Miao Jiang,Corina Nantais, Linyan wan, Ryousuke Akutsu, Yousuke Ashida, Yutaro Sonoda, Akira Takenaka.

And I also thank for the Super Kamiokande experiment group and the T2K experiment group.

I also thank for the teachers and students of Okayama University. Special thanks go to Hirokazu Ishino, Ou Iwa, Shintaro Ito, Tubasa Kayano, Xu Chenyuan, Tetsuya Shirahige, Yousuke Kida, Kaito Hagiwara, Hirotaka Nagata.

There are too many people whose I appreciate. I could not write all people. Thanks to all of the people.

Finally, I am grateful for my family and friends who supported my life. Thank you very much.

Contents

	Fermions			Bosons	
	I	II	III	Gauge	Scaler
Quarks	u (Up)	c (Charm)	t (Top)	g (Gluon)	H (Higgs)
	d (Down)	s (Strange)	b (Bottom)	γ (Photon)	
Leptons	e (Electron)	μ (Muon)	τ (Tau)	Z (Z boson)	
	ν_e	ν_μ	ν_τ	W(W boson)	

Figure 1: Twelve Standard Model fermions (including six leptons and six quarks.) and five standard model bosons.

1 Introduction

Elementary particles are components of matter that have no internal structure. There are currently two known types of elementary particles: leptons and quarks. Atoms, molecules, and other constituents of matter are formed by combining these elementary particles. There are four types of interactions - strong, weak, electromagnetic, and gravitational which are carried out by interaction carriers. Quarks are subject to all four interactions, and charged leptons are subject to weak, electromagnetic, and gravitational interactions. By contrast, neutral leptons are subject to weak and gravitational interactions and are called neutrinos. In particle physics, the gravitational interaction is ignored as its effect is very small. The theory summarizing these interaction is called the Standard Model and an outline is presented in Figure 1. In this model, the mass of neutrino is set to 0.

1.1 Neutrinos

In 1933, the neutrino was proposed from β decay bu Wolfgang Pauli and named by Enrico Fermi. In 1965, it was discovered by Cowan and Reines. Thereafter, the Kamiokande observed the supernova neutrino, and the SK demonstrated the neutrino have mass.

Neutrinos have a low interaction cross-section with other elementary particles: their, detection is therefore difficult, requiring a large detector and a high flux neutrino beam.

There are currently three neutrino flavors, that have been confirmed: ν_e, ν_μ and ν_τ, and their antiparticles, $\overline{\nu}_e, \overline{\nu}_\mu$ and $\overline{\nu}_\tau$. Each flavor of neutrino has a charged lepton partner. which is e^-, μ^- and τ^-, and antiparticle e^+, μ^+ and τ^+. Neutrinos have several interesting features, such as neutrino oscillation, which is explained in Section 1.2.

1.2 Neutrino oscillation

Three types of neutrino, namely ν_e, ν_μ and ν_τ, change with time, a phenomenon that referred to as neutrino oscillation[1], [2]. Neutrino oscillation is caused by differences in flavor state, ν_e, ν_μ and ν_τ, and mass state, ν_1, ν_2 and ν_3. Neutrino mass is represented by the quantum superposition of the three masses of neutrinos. Although the eigenstate of this mass takes time, its type does not change. However, the weight of the superposition changes, and at that time, the type of eigenstate of the flavor changes. Expressed mathematically, a neutrino flavor is denoted $|\nu_\alpha\rangle$ ($\alpha = e, \nu, \tau$). When the neutrino mass is denoted as $|\nu_i\rangle$ ($i = 1, 2, 3$), the matrix is represented by

$$|\nu_\alpha\rangle = \sum_i U_{\alpha,i} \, |\nu_i\rangle \tag{1}$$

where, U_α, i is called a PSMN matrix (for Pontecorvo, Maki, Nakagawa and Sakata) [3] and written as follows:

$$\begin{aligned} U_{\alpha,i} &= \begin{pmatrix} U_{e,1} & U_{e,2} & U_{e,3} \\ U_{\mu,1} & U_{\mu,2} & U_{\mu,3} \\ U_{\tau,1} & U_{\tau,2} & U_{\tau,3} \end{pmatrix} \\ &= \begin{pmatrix} c_{12}c_{13} & s_{12}c_{13} & s_{13}e^{-i\delta} \\ -s_{12}c_{23} & -c_{12}s_{23}s_{13}e^{i\delta} & c_{12}c_{23} - s_{12}s_{23}s_{13}e^{i\delta}s_{23}c_{13} \\ s_{12}s_{23} & -c_{12}c_{23}s_{13}e^{i\delta} & -c_{12}c_{23} - s_{12}c_{23}s_{13}e^{i\delta}c_{23}c_{13} \end{pmatrix} \end{aligned} \tag{2}$$

where $s_{ij} = \sin\theta_{ij}$, $c_{ij} = \cos\theta_{ij}$ and θ_{ij} are the mixing angles, and δ is the CP violation for the Dirac neutrino phase. The time evolution of each mass eigenstate is the following Schrodinger equation: and is written as follows:

$$i\frac{d}{dt}\,|\nu_i(t)\rangle = \mathcal{H}\,|\nu_i(0)\rangle \tag{3}$$

$$|\nu_i(t)\rangle = e^{-iE_it}\,|\nu_i(0)\rangle \tag{4}$$

where E_i is the neutrino energy. In addition, the time evolution of each flavor eigenstate is written as follows:

$$|\nu_\alpha(t)\rangle = \sum_i U_\alpha, ie^{-iE_it}\,|\nu_i(0)\rangle = \sum_{i,\beta} U_{\alpha,i}U^*_{\beta,i}e^{-iE_it}\,|\nu_\beta(0)\rangle \tag{5}$$

The neutrino momentum, P, is much heavier than the neutrino mass, m:

$$E_i = sqrt(p^2 + m_i^2) \simeq P + \frac{m_i^2}{2p} \simeq p + \frac{m_i^2}{2E_i} \tag{6}$$

Therefore, the oscillation probability of a neutrino of flavor α, ν_α, is changed to ν_β

$$\begin{aligned} P(\nu_\alpha \to \nu_\beta)(t) &= \langle \nu_\beta | \, |\nu_\alpha(t)\rangle^2 \\ &= \left| \sum_i U_{\alpha,i} U^*_{\beta,i} e^{-iE_i t} \right|^2 \\ &= \sum_{i,j} U_{\alpha,i} U^*_{\beta,i} U^*_{\alpha,j} U_{\beta,j} e^{-i(E_i - E_j)t} \\ &= \sum_i |U_{\alpha,i}|^2 |U_{\beta,i}|^2 + U^*_{\alpha,j} U_{\beta,j} e^{-i(E_i - E_j)t} \end{aligned} \tag{7}$$

Then, t can be approximated by $t \simeq L$ because the neutrino mass is very small and its velocity is close to the speed of light:

$$P(\nu_\alpha \to \nu_\beta)(L) = \sum_{i,j} |U_{\alpha,i} U^*_{\beta,i}|^2 + 2Re \sum_{i>j} U_{\alpha,i} U^*_{\beta,i} U^*_{\alpha,j} U_{\beta,j} e^{-i\frac{\Delta m^2_{ij} L}{(2E)}} \tag{8}$$

where $\Delta m^2_{ij} = m^2_1 - m^2_2$. Thus, the probability $\nu_\mu \to \nu_\mu$ that ν_{mu} survives when flying at a distance of L in a vacuum is approximated as

$$P(\nu_\alpha \to \nu_\beta)(t) \simeq \sin^2(2\theta_{13}) \sin^2\theta_{23} \sin^2(\frac{1.27\Delta m^2_{13} L}{E_\nu}) \tag{9}$$

Here, the phase factor is written as follows:

$$\Delta_{ij} = \frac{\Delta m^2_{ij} L}{4E_\nu} = 1.27 \frac{\Delta m^2_{ij}}{E_\nu} \tag{10}$$

Then, the oscillation probability of $\nu_\mu \to \nu_e$ is written as

$$\begin{aligned} P(\nu_\nu \to \nu_e)(t) &= 4c^2_{13} c^2_{13} s^2_{23} \sin^2 \Delta_{31} \\ &+ 8c^2_{13} s_{12} s_{13} s_{23} (c_{12} c_{23} \cos\delta - s_{12} s_{13} s_{23}) \cos\Delta_{32} \sin\Delta_{31} \sin\Delta_{21} \\ &- 8c^2_{13} c_{12} c_{23} s_{12} s_{13} s_{23} \sin\delta \sin\Delta_{32} \sin\Delta_{31} \sin\Delta_{21} \\ &+ 4s^2_{12} c^2_{13} (c^2_{12} c^2_{23} + s^2_{12} s^2_{23} s^2_{13} - 2c_{12} c_{23} s_{12} s_{23} s_{13} \cos\delta) \sin^2\Delta_{21} \\ &+ 8c^2_{13} s^2_{13} s^2_{23} (1 - 2s^2_{13}) (\frac{a}{\Delta m^2 31} sin^2 \Delta_{31} - \frac{aL}{4E_\nu} \cos\Delta_{32} \sin\Delta_{31}) \end{aligned} \tag{11}$$

where, a is the mass effect. The first term of the equation is the leading term, therefore the neutrino oscillation probability is approximated as follows:

$$P(\nu_\nu \to \nu_e)(t) \simeq 4c^2_{13} c^2_{13} s^2_{23} \sin^2 \Delta_{31} \tag{12}$$

The anti-neutrino oscillation probability is calculated by inverting the signs of a and δ. Thus, the CP violation phase in the lepton sector is measured by the difference of $\nu_\nu \to \nu_e$ and $\overline{\nu_\nu} \to \overline{\nu_e}$. CP violation in the lepton may provide important clues for understanding the asymmetry between matter and antimatter in the universe.

1.2.1 Neutrino oscillation parameters

The neutrino oscillation parameters have been summarized by the Particle Date Grope based on past experimental results[4]. In this thesis, the neutrino oscillation parameters are taken from PDG2018 and summarized in the Table 1.

Table 1: Oscillation parameters[4]. In this thesis, Normal Hierarchy and $\delta_{CP} = 0$.

Parameter	Best-Fit	3σ
$\Delta m^2_{21}[10^{-5}\ \mathrm{eV}^2]$	7.37	6.93 - 7.96
$\Delta m^2_{31}[10^{-3}\ \mathrm{eV}^2]$	2.56	2.35 - 2.69
$\sin^2\theta_{12}$	0.297	0.250-0.354
$\sin^2\theta_{23}, \Delta m^2_{31}$	0.425	0.381-0.615
$\sin^2\theta_{13}, \Delta m^2_{31}$	0.0215	0.0190-0.0240

1.3 Neutrino-neucleus interaction

There are two types of neutrino-nucleus interactions: charged current and neutral current interactions. In this thesis, a neutral current quasi elastic interaction, which is a type neutral current interaction, is addressed.

1.3.1 Charged Current

The charged current interaction was first discovered by Cowan and Reines and can be described as follows: $\nu_e + p \rightarrow e^+ + n$[5]. In this interaction, neutrino absorb the W^+ boson and then generate charged leptons of the same flavor. In principle, this interaction is easily observed because charged particle are emitted. In addition, charged current interaction cross-section is generally larger than that of neutral current interactions. As a result, the SK, which is primary detector addressed in this thesis, detects a greater number of charge current events than neutral current events.

1.3.2 Neutral Current

Neutral Current interaction was discovered in a bubble chamber in the Gargamelle experiment in 1973 [6]. In this interaction, neutrinos absorb the Z^0 boson, and transfer energy and momentum to a nucleon or nucleus: the neutrinos themselves are not affected by this interaction. Generally, a neutral current interaction is observed by the measurement of track by matter, which provides the energy and momentum.

1.3.3 Quasi-elastic scattering

Neutral current and charged current interactions often involve nucleons in the nucleus. This interaction is called quasi-elastic scattering. When the neutrino energy

is in the sub-GeV region, $0.1 < E_\nu < 1$ GeV, the quasi-elastic scattering cross-section by matter is larger than that of non quasi-elastic scattering. Thus, in the SK, quasi-elastic scattering is detected more often than non quasi-elastic scattering. In particular, neutrino-oxygen neutral current quasi-elastic(NCQE) scattering is observed, which is the main interaction examined in this thesis.

1.3.4 Supernova Relic Neutrino

There are 10^{21} stars in the universe. Among these, 10^{17} have a solar mass of greater than 8M and are expected to ultimately generate a supernova explosion[11]. From the beginning of the universe, many stars have resulted in supernova explosions. In a supernova explosion, 1% of the total energy is carried by light and 99% is emitted by neutrinos. Thus, neutrinos from past supernovas are present in the current universe and are referred to as SRNs[7]. SRNs have been proposed by various theories and have been observed in experiments such as the SK[8], [9]. However, they have not yet been observed by the SK. Thus, SK-Gd project starte in SK. SK-Gd is discussed in Section 2.4.5.

1.4 Thesis overview

This thesis reports the NCQE cross-section measurement by the T2K experiment in Run1 to 4, as well as the measurement of the multiplicity and ration of neutron knocked out of an oxygen nucleus via the NCQE interaction. Figure 2 presents a schematic of this interaction. This interaction can be observed via de-excitation gamma ray that is emitted from an oxygen nucleus that has lost a nucleon.

1.4.1 History of NCQE interaction measurement

The observation of the water-neutrino NCQE interaction was first attempted in the K2K experiment. In this experiment, ν_μ neutrinos with an average energy of 1.3 GeV were generated and detected by a 1 kton water Cherenkov detector [10]. Figure 3 depicts the 1 kton water Cherenkov detector. A peak of approximately 6 MeV was discovered in this experiment, as presented in Figure 4. However, the experiment did not study the theory of the NCQE cross-section or de-excitation of oxygen. As a result, the K2K experiment did no provide NCQE cross-section measurement or consequences such as secondary neutrons. The NCQE interaction was quantitatively measured for the first time in T2K experiments [12]. In this thesis, the NCQE cross-section is measured in greater detail with the help of increased statistical numbers and improved simulations. In addition, neutron via the NCQE interaction by the T2K beam are measured for the first time.

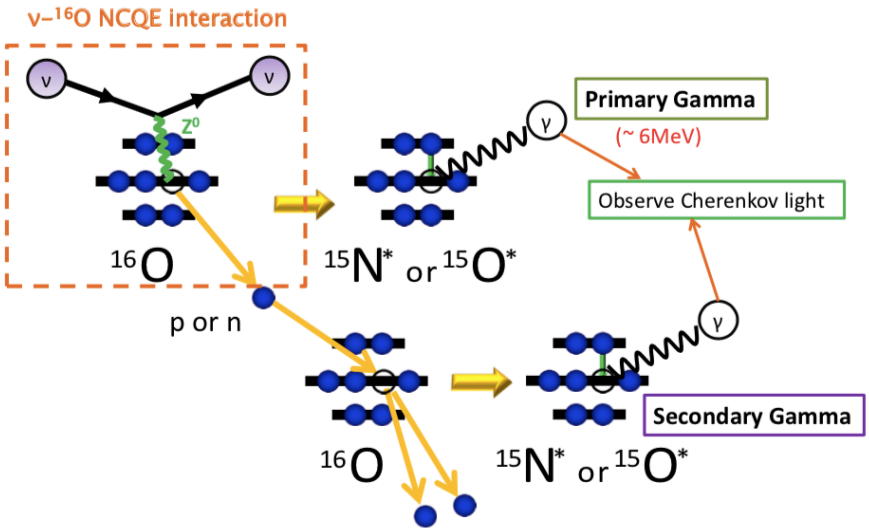

Figure 2: Schematic of a neutrino-oxygen NCQE interaction. In the SK, the NCQE interaction is observed via a de-excitation gamma ray.

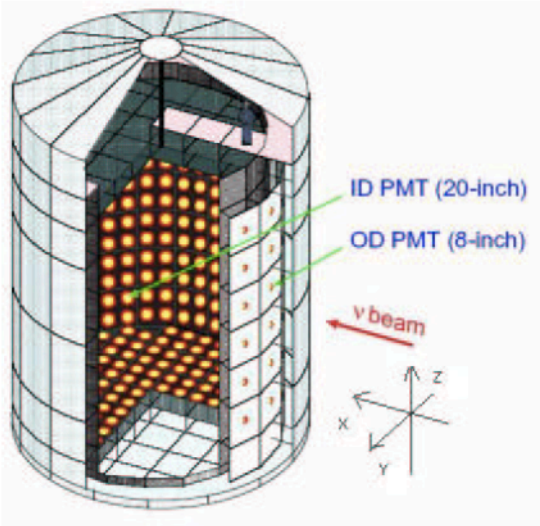

Figure 3: Schematic view of the 1 kton water Cherenkov detector used by the K2K near detector[10].

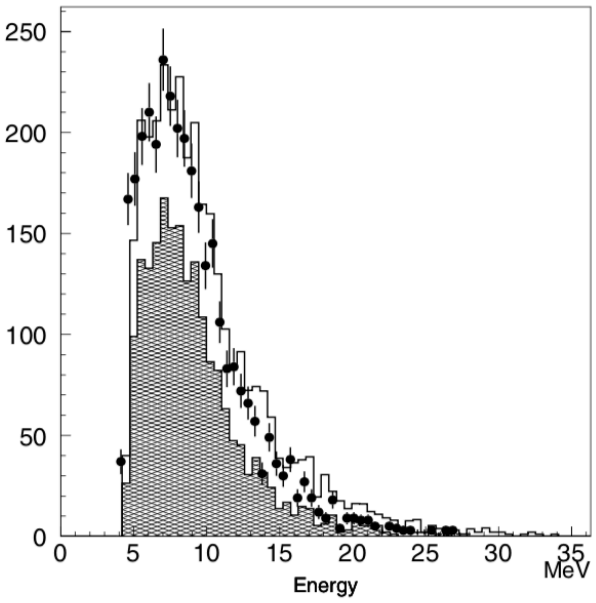

Figure 4: Energy distribution using the 1 kton detector [10]. Dots represent the data point, and the histogram illustrates the expected gamma-ray energy distribution by MC. The hatched histogram represents the expected de-excitation gamma-rays from the NCQE interaction.

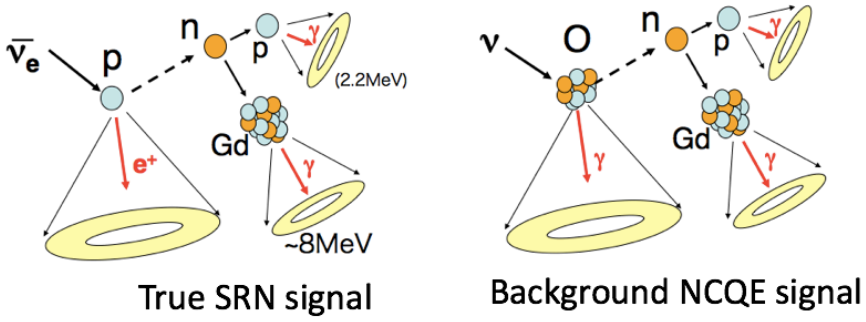

Figure 5: Schematic view the SRN and NCQE signals in the SK-Gd. Left image depicts the SRN inverse beta decay in the Sk-Gd, and the right image depicts the NCQE via a single neutron signal in the SK-Gd.

1.4.2 NCQE interaction measurement motivation

The main motivation for measuring the NCQE cross-section is to aid in the future discovery of SRNs in the SK-Gd. An NCQE interaction with a single neutron from atmospheric neutrinos is one of main contributors to the background in SRN searches, as described in Section 2.4.5. Figure 5 presents the SRN signal and NCQE interaction signal in the SK-Gd. As shown in this figure, both signals are similar to one another and cannot be discovered by the Sk-Gd, it is necessary to precisely measure the NCQE cross-section and neutron multiplicity from the NCQE interaction. The measurement result of the NCQE cross-section are presented in Section 6, and the result of neutron tagging are presented in Section 7.3.1.

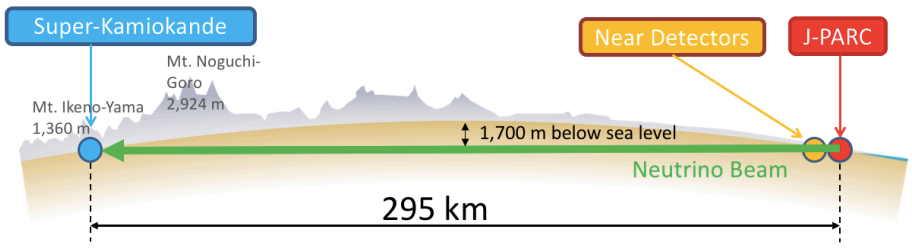

Figure 6: Schematic of the T2K experiment[13].

2 Experiment

2.1 T2K experiment

The T2K(Tokai-to-Kamioka) experiment is a long baseline neutrino oscillation experiment [13]: its overview is presented in Figure 6. The main purpose of this experiment is to measure the neutrino oscillation parameters by $\nu_\mu \to \nu_e$ oscillation [14]. In the experiment, neutrinos are generated by the Japan Proton Accelerator Research Complex (J-PARC) in Tokai village. The neutrino beam is produced 2.5° off-axis, and the neutrinos are detected at the far detector, SK, at a distance of 295 km from J-PARC. This experiment has a two near detectors that are installed 280 m downstream from the neutrino generation target.

2.2 J-PARC

The J-PARC consists of proton accelerators and laboratory facilities that are used to conduct research in fields such as particle physics, nuclear physics, material science and life science. Figure 7 presents an overview of the facilities at the J-PARC. Among these, the T2K experiment uses a proton beam for generating a 2.5° off-axis neutrino beam. The 2.5° off-axis method leads to peak neutrino energy at approximately 630 MeV. The neutrino energy maximia of $\nu_\mu \to \nu_e$ neutrino oscillation at 295 km. ν_μ are generated by pion decay. The energy of a neutrino with each off-axis angle is derived as follows:

$$E_\nu = \frac{m_\pi^2 - m_\mu^2}{2(E_\pi - p_\pi \cos\theta_{OA})} = \frac{m_\pi^2 - m_\mu^2}{2p_\pi(\frac{1}{\beta_\pi} - \cos\theta_{OA})} \tag{13}$$

where E_ν and E_π are the neutrino and pion energies, respectively, m_π and m_μ are the pion and muon masses, respectively, θ_{OA} is the off-axis angle, and p_π is the pion momentum. This demonstrates that, when the off-axis angle increases, the neutrino energy is close to monochromatic. As a result, the neutrino oscillation probability at $\nu_\mu \to \nu_e$ at 295 km in the T2K is demonstrated in Figure 8: it reaches a maximum at approximately 630 MeV.

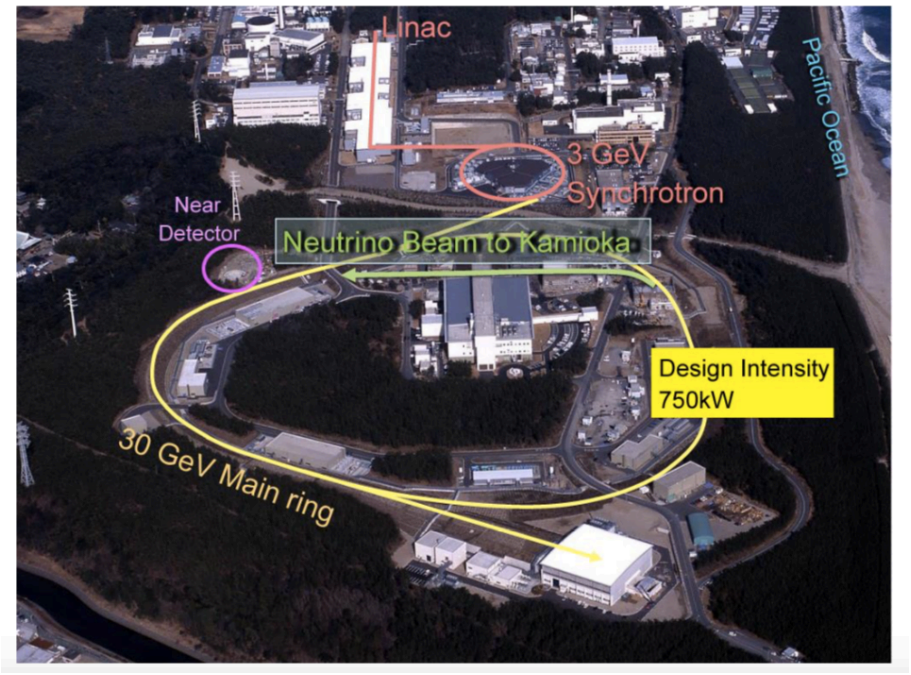

Figure 7: Aerial photograph of the J-PARC.

2.2.1 J-PARC proton beam

The J-PARC consists of three types of accelerators: a linear accelerator (LINAC), a rapid-cycling synchrotron (RCS) and a main ring (MR). The LINAC produces 400 MeV H^--ions, which are converted to H^+ ions (protons) by charge-stripping foils prior to injection into the RCS. These protons are then accelerated to 30 GeV in the RCS. Then, approximately 5% of the these 30 GeV protons are delivered to the MR.

2.2.2 Primary beam-line

The primary beam-line is used for a neutrino beam only and is depicted in Figure 9. This beam generated by the MR is measured by multiple monitors in the primary beam-line as described below.

- Current transfer (CT):

  The proton beam intensity and timing are measured by five current transfers(CT). CT monitors consist of a 50-turn coil of copper wire and measure coil current by the proton beam. The resolution of the monitors is better than 10 ns.

- Electro-static monitor (ESM):

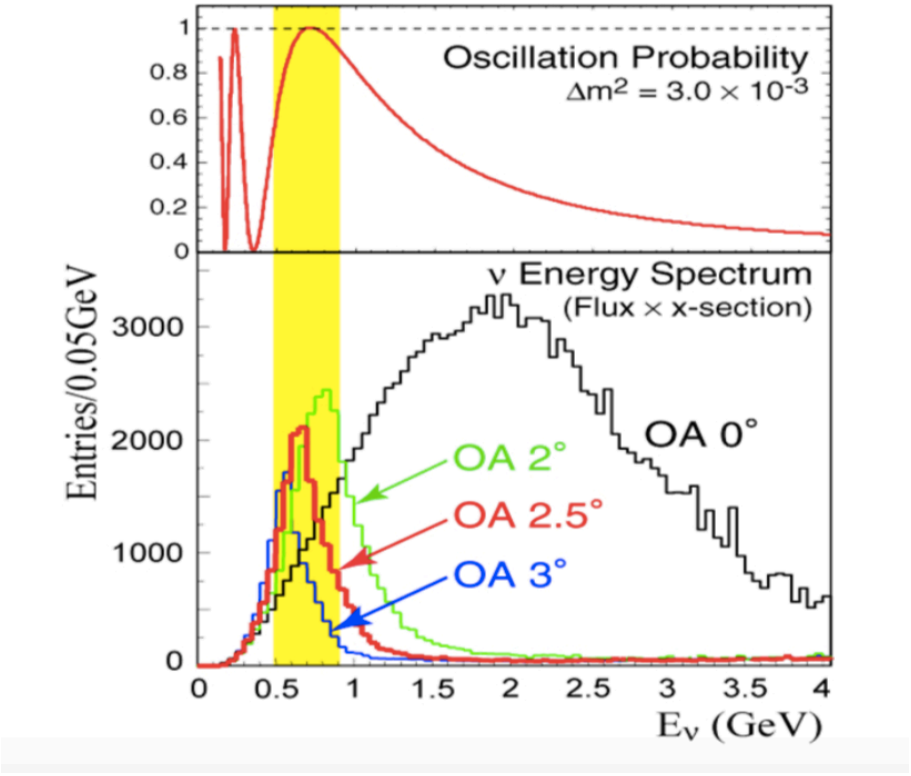

Figure 8: The upper graph illustrates oscillation probability. $\nu_\mu \rightarrow \nu_e$ is at a maximum at approximately 630 MeV and an off-axis angle of 2.5° at a distance of 295 km. The lower histogram illustrates the energy spectrum of neutrinos with each off-axis angle at a distance of 295 km [13].

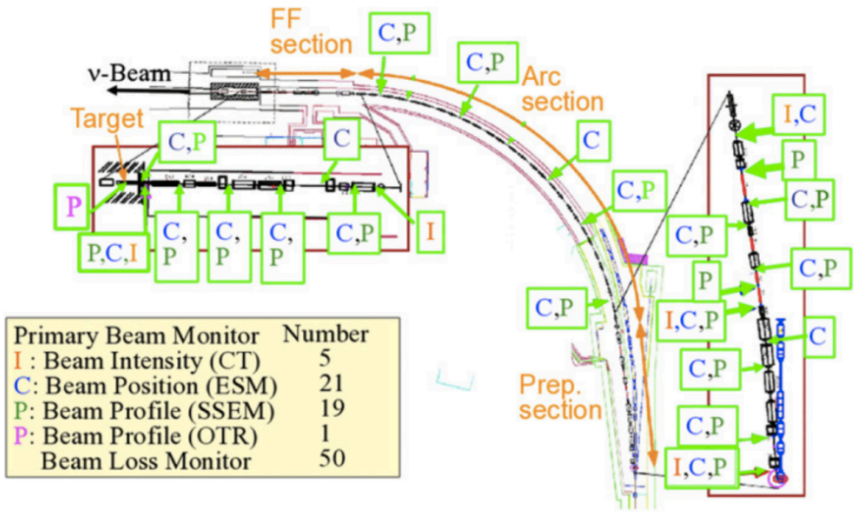

Figure 9: Schematic of the PrimaryBeamline

The center position of the proton beam is non-destructively measured by 21 electrostatic monitors(ESM). Each ESM consists of four circular rectangular electrodes, with the electrodes are arranged around the proton beam orbit. The beam position is measured by the four electrode currents. The measurement resolution of the beam center position has a value less than 450 μm.

- Segmented secondary emission monitor (SSEM):

  The profile of the proton beam is measured by 19 segmented secondary emission monitors(SSEM). Each SSEM is composed of two thin titanium foil strips and an anode HV foil between the strips. The titanium foil strip is installed horizontally and the anode HV foil is installed vertically. When a proton beam passes the strips, each strip emits the electrons in proportion to the beam flux. The electrons drift along the electric field into the anode foil: this drift process induces currents on the strip. The beam profile is reconstructed from the corrected charge distribution. The uncertainty of the beam width measurement by SSEM is 700 μm.

- Beam loss monitor (BLM):

  Leakage of the proton beam near the beam pipe is detected by 50 beam loss monitors (BLM). Each BLM is a linear proportional counter filled with an $Ar - CO_2$ mixture. Signals are integrated during the outflow. When a signal exceeds the threshold, a beam abort interlock signal is fired. A BLM can detect a beam loss up to 16 mW.

After measurement by these monitors, the proton beam is delivered to the graphite target.

2.2.3 Target

The secondary beam-line, illustrated in Figure 10, includes the target, magnetic horn, decay volume and beam dump, and it is located downstream of the primary beam line. The beams that pass through the primary beam line are provided to the target. the target core, depicted in Figure 11, is a graphite rod with a length of 91.4 cm and a diameter of 2.6 cm. The graphite rod has a density of 1.8 g/cm^3 and is covered by a titanium case with a thickness of approximately 0.3 mm. Hadrons, such as pions and kaons, are generated through the interaction between the proton beam and graphite, and they then fly to the magnetic horn.

2.2.4 Magnetic horn

The T2K uses three magnetic horns [15], [16], each consisting of two coaxial inner and outer conductors. The conductor surrounds the closed volume in which the toroidal magnetic field is generated. The first horn focuses a relatively large angle

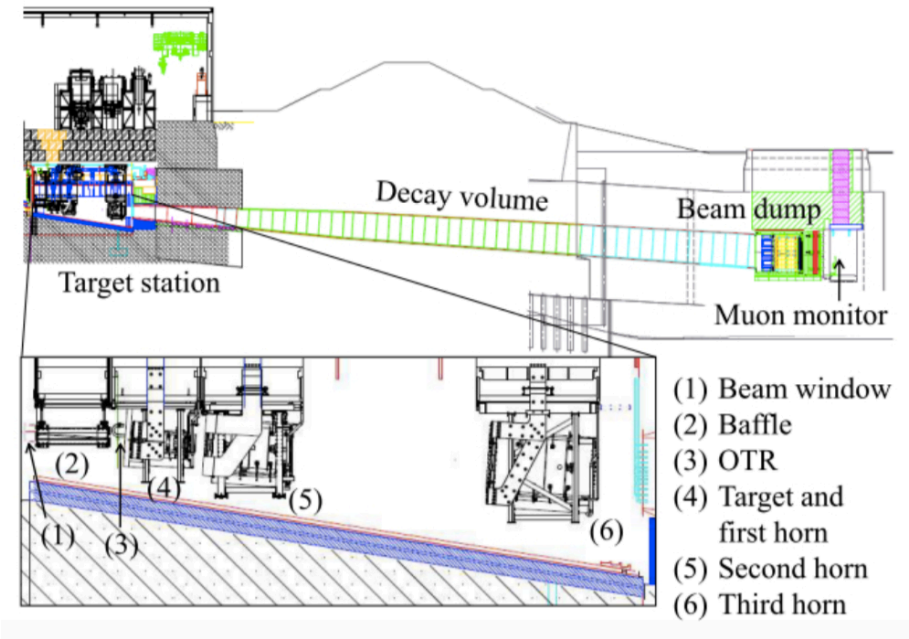

Figure 10: Diagram of the secondary beam line.

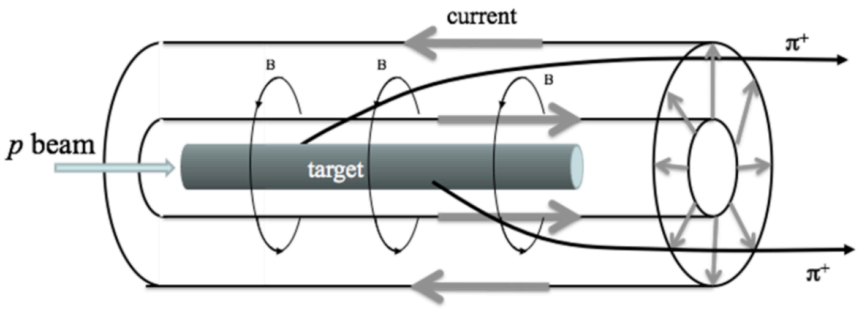

Figure 11: Schematic of the Target.

pion, and the second and third horns focus the other pions. When the T2K beam is in ν mode, the positive pion is focused by the horn and the negative pion is defocused. By contrast, When T2K beam is $\overline{\nu}$ mode, negative pion is focused by the horn, and the positive pion is defocused. The focused pions then fly the decay volume.

2.2.5 Decay Volume

The decay volume is a 96 m iron tunnel surrounded by a 6 m thick reinforced concrete shield. Within this volume, hadrons (pions and kaons) decay into neutrinos and muons.

2.2.6 Beam dump

At the end of the decay volume, there is a beam dump consisting of 75 tons of graphite blocks that are 3.174 m long, 1.94 m wide, and 4.69 m high. The beam dump stops all particles, except the neutrinos and high energy muons of more than approximately 5 GeV.

2.2.7 Muon monitor

A muon monitor, illustrated in Figure 12, is located after the beam dump and measures the muon intensity and profile. The muon monitor consists of two types of detector arrays: ionization chambers and silicon PIN photodiodes. Each array has 49 sensors at 25 cm $\times$ 25 cm intervals and covers a 150 $\times$ 150 cm^2 area. The muon profile is reconstructed into two dimensions in each array for each spill. The monitor has a muon intensity resolution of approximately 0.1% and a direction resolution of approximately 0.2 mrad.

2.3 Near Detector

There are two types of near detectors that are installed approximately 280 m downstream from the target: the Interactive Neutrino Grid (INGRID) detector, which measures the neutrino beam direction and intensity of each off-axis, and ND280, which measures the neutrino properties with the same off-axis as the SK. Figure 13 illustrates the detectors.

2.3.1 INGRID

Figure 14 depicts the INGRID detector [17], which is composed of 16 identical modules. Fourteen modules are arranged horizontally and vertically in a cross shape, and the central detectors of each axis are installed so as to overlap at the beam center (off-axis of 0°). The remaining two modules are generally not used for analysis. The INGRID detector is a sandwich structure in which iron target layers and

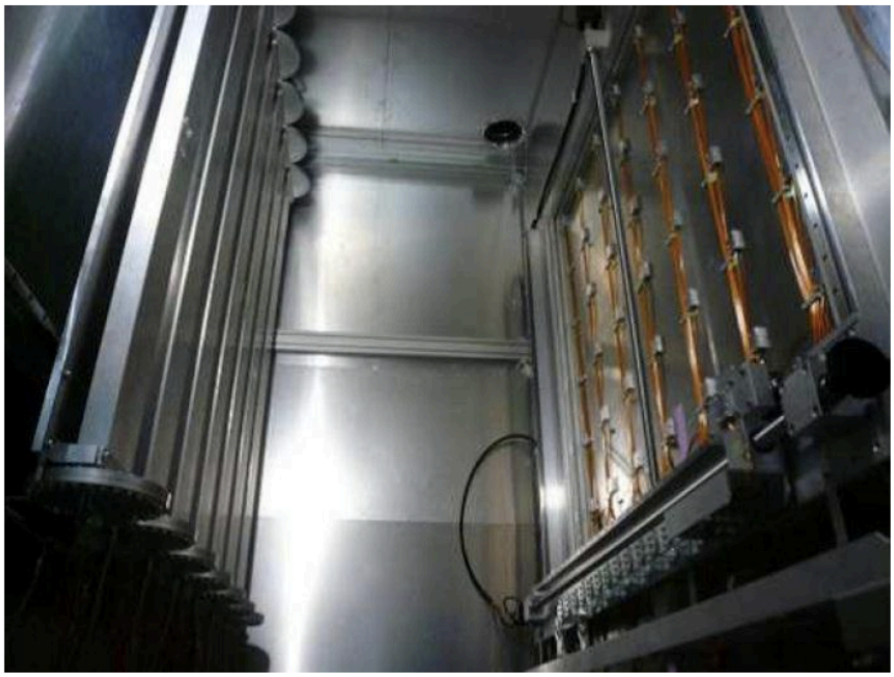

Figure 12: Image of the muon monitor.

scintillator layers are alternately arranged. The iron targets (neutrino targets) have nine layers, and the scintillator has 11 layers. Charged particles are generated by the interaction between iron and the neutrinos, and they pass through the scintillator, generating scintillation light. The scintillation light is detected by photosensors and reconstructed: the neutrino beam profile is thereby detected. As a result, the beam center center can be determined at approximately 10 cm, implying that the detector has a precision of approximately 0.4 mrad.

2.3.2 ND280

The ND280 detector is installed at an angle of 2.5° from the beam center [18]. Figure 15 presents a diagram of the detector. The ND280 is 7.6 × 5.6 × 6.1 m in size and consists of subdetectors. In the center, there are trackers, including two Fine Grained Detectors (FGD) and three TPCs. In addition, an π^0 detector is installed upstream of the tracker and is surrounded by multiple Electromagnetic Calorimeter.

2.4 Super-Kamiokande

Figure 16 presents an overview of the Super-Kamiokande(SK) [19]. The SK consists of a large water Cherenkov detector with two layers that uses 50 kt of pure water. It is located in the city of Hida in Gifu, Japan. The main purpose of the SK is the

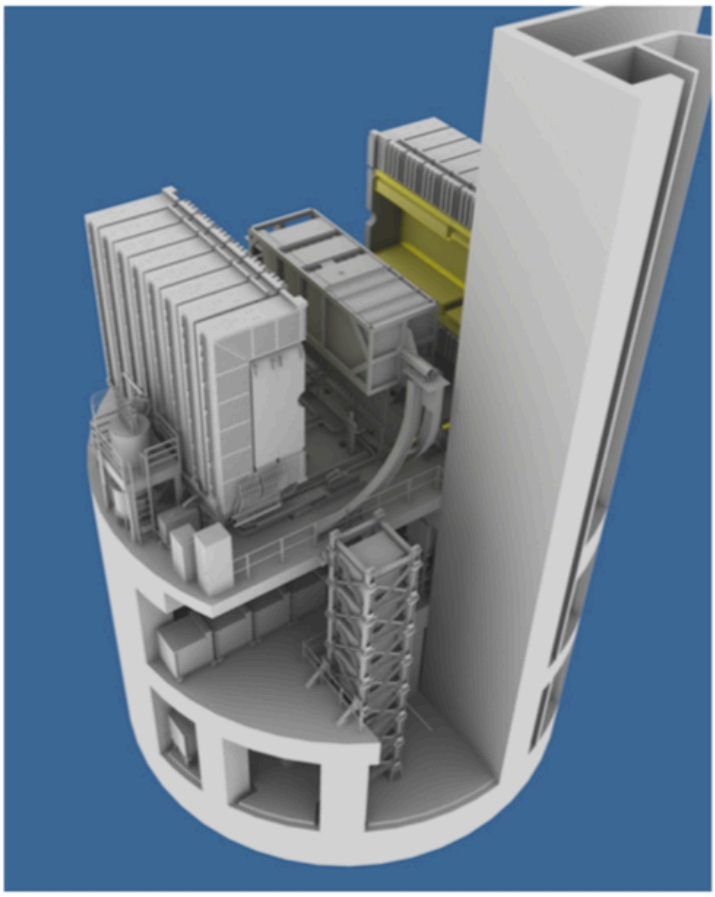

Figure 13: Visualization of the near detector. The center of the INGRID module is installed at the SS floor(middle level), and ND280 is installed at the B1 floor (upper level).

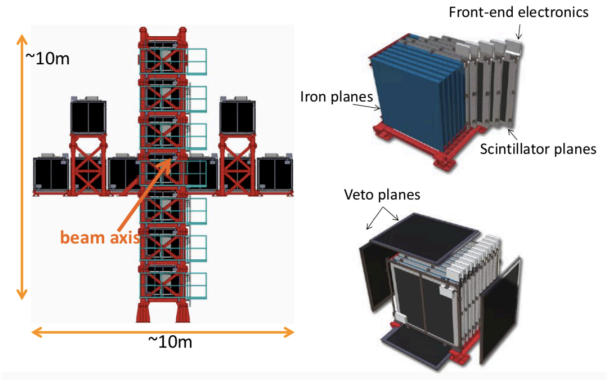

Figure 14: INGRID detector. The left image illustrates the installation positions of the 16 INGRID modules.

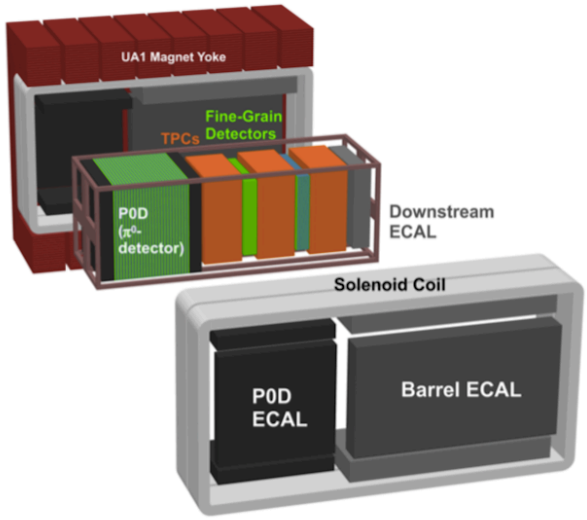

Figure 15: Diagram of ND280.

discovery of proton decay and the observation of neutrinos. In the SK, a total of 11,129 of 20 inch Photomultiplier Tube(PMT) [20] are installed in the inner water tank, providing 40% photo-coverage. And, 1,885 of 8 inch PMT are installed in the outer water tank. Figure 16 depicts the SK, which is located 1,000 m underground for the bedrock to reduce background signals such as cosmic rays. The SK is sensitive to a wide energy band from approximately several TeV, which is a high energy region, to several MeV, which is a relatively low energy region.

The performance of the PMTs is affected by the magnetic force. Therefore, a Helmholtz coil is placed around the SK tank to nullify the geomagnetic field. The Helmholtz coil serves to reduce the influence of geomagnetism to less than 100 mG, and the performance of each PMT is uniform.

2.4.1 Structure

Fifty kilotons of pure water are contained in a stainless steel cylindrical tank that is 39.3m in diameter and 41.4m in height. The tank is partitioned into an inner detector (ID) containing 20 inch PMT and an outer detector (OD) containing 8 inch PMT. The two zones are separated by a 55 cm thick stainless steel support structure to which the PMTs are attached as illustrated in Figure 17.

- Inner Detector The Inner Detector(ID) is a cylinder with a hight of 36.2 m and a diameter of 33.8 m and contains pure water. There are 11,146 20 inch PMTs (Hamamatsu R3600) installed in the center of the tank, 7,650 along the ID wall of the tank, 1,784 on the top of the tank, and 1,748 on the bottom

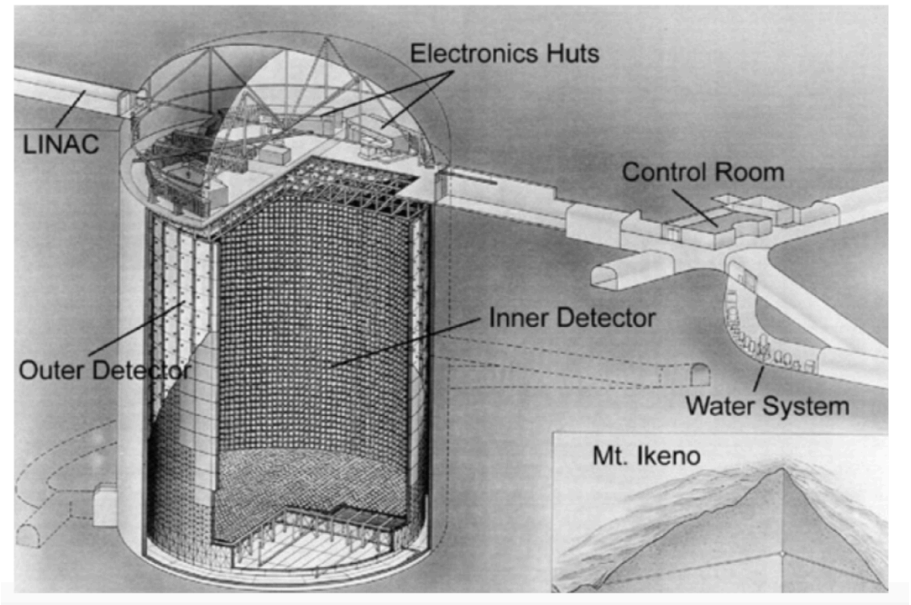

Figure 16: Schematic view of the Super-Kamiokande.

of the tank: the PMTs are attached to a 70 cm grid. PMTs are described in greater detail in Section 2.4.3. The photo coverage of the ID surface is 40%. The remaining 60% of the surface is covered by black sheet, as these minimize the background by photo reflection and optically separate the ID and OD.

- Outer Detector The Outer Detector(OD) contains pure water as well and surrounds the ID. It has a cylindrical shape with a heigh of 36.2 m and a diameter of 33.8 m. the OD thickness or the distance between the walls of the OD and ID is approximately 2.05 m on the top and bottom of the detector and 2.2 m on the barrel wall. There are 1,885 8 inch PMTs (Hamamatsu R1408) installed on the outside of the ID wall facing the OD wall, 1,275 on the outside of the ID wall, 302 on the top of the wall and 308 on the bottom of the wall.

  The OD is primarily used to reject charged particles such as cosmic ray muons. Neutrinos do not emit when passing through the OD, but charged particles emit Cherenkov light. Thus, when the PMTs of the OD are hit, neutrinos are not involved. In addition, the surface of the OD is attached to white Tyvek sheets that reflect Cherenkov light by more than 80%: this enhances the efficiency of Cherenkov light collection.

2.4.2 Cherenkov Radiation

SK reconstructs physics events is such as Cherenkov radiation, which is the light emitted when relativistically charged particles pass through a medium at a speed

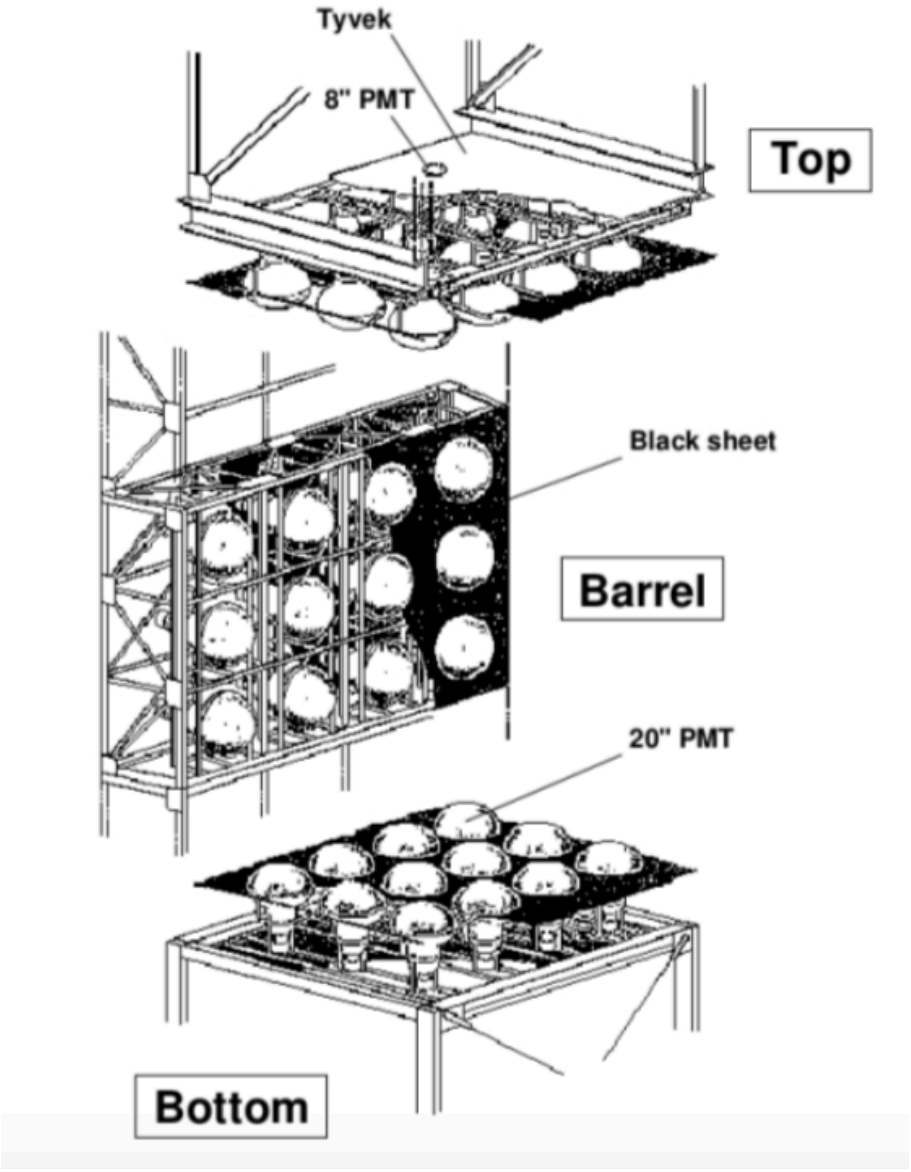

Figure 17: Illustration of the PMT support structures.

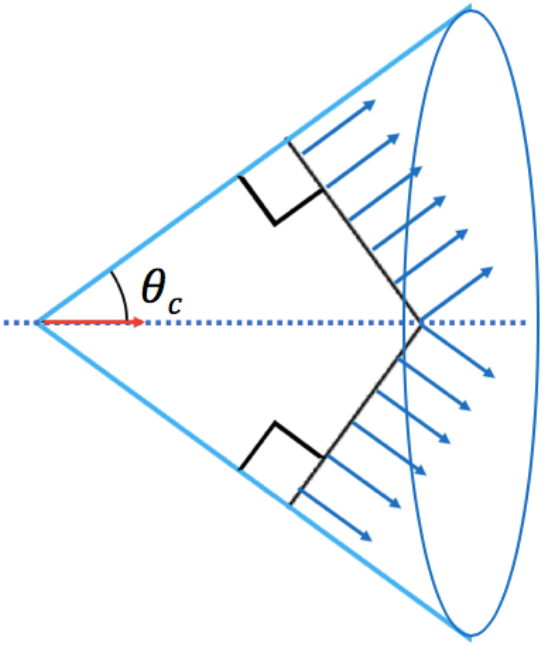

Figure 18: Diagram of the Cherenkov radiation, where θ_C is the Cherenkov angle.

greater than that of light in that medium. Figure 18 presents an overview of Cherenkov radiation. The radiation conditions involve a simple inequality:

$$\beta > \frac{1}{n} \tag{14}$$

where $\beta = v/c$, v is the particle speed and n is the fraction index of the material. In pure water in the SK, $n = 1.33$, therefore $1/n \approx 0.75$. Cherenkov light is emitted at an acute angle to the direction in which the particles move. The light spreads like a cone, and as depicted in Figure 18, the half-angle θ_C is commonly referred to as the Cherenkov angle. The Cherenkov angle is expressed as the following inequality:

$$\cos(\theta_C) = \frac{1}{n\beta} \tag{15}$$

where the relativistic limit speed $\beta \approx 1$, Cherenkov angle, θ_C, is the maximum angle, 42°. The Cherenkov angle provides critical information for distinguishing types of particles. The Cherenkov angle of electrons and high energy heavy particles, such as muons, pions and protons, are 42°. However, when heavy particles hove insufficient momentum, the Cherenkov angle decreases. In addition, when the momentum decreases further, Cherenkov light is not emitted because the particles' relativistic speed is below the speed of the light in pure water. The function of the mass and Cherenkov light threshold is calculated as follows:

$$p_{thr} = \frac{m}{\sqrt{n^2 - 1}} \tag{16}$$

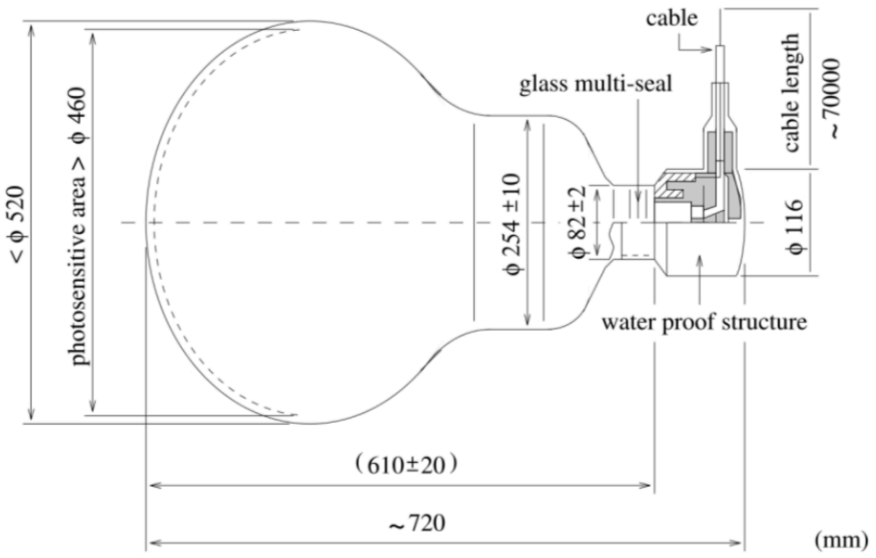

Figure 19: Schematic of a 20 inch PMT, R3600.

where p_{thr} is represent the momentum threshold of each particle and m represents particle mass. As a result, the Cherenkov threshold of the particles is as follows: $e^{\pm}$ are 0.58 MeV/c , $\mu^{\pm}$ are 121 MeV/c, $\pi^{\pm}$ are 159 MeV/c, and $K^{\pm}$ are 563 MeV/c.

The emitted Cherenkov photons have a wavelength dependence and are descruved as follows:

$$\frac{d^2N}{dxd\lambda} = \frac{2\pi\alpha}{\lambda^2}(1 - \frac{1}{n^2\beta^2}) \tag{17}$$

where N is the number of emitted photons, λ is the wavelength, α is structure constant, and x is the distance of particle transfer. In the sensitive wavelength range of a Super-Kamiokande PMT(SKPMT: 300-600 nm), approximately 340 photons are emitted per centimeter of travel. The SKPMT is described in Section 2.4.3.

2.4.3 Photomultiplier Tube

The ID uses Hamamatsu R3600, SKPMT, that are 20 inch diameter and have venetian blind dynodes. Figure 19 presents a diagram of the SKPMT. The photocathode in the SKPMT is coated with Bi-alkali (Sb-K-Cs) on the glass inner surface, which tends to cause a photoelectric effect. In particular, SKPMT Bi-alkali is composed of materials with optimal quantum efficiency (QE) for 300 to 600 nm, which is the Cherenkov wavelength range in water. Figure 20 illustrates the relationship between QE and wavelength: the region from 360 to 400 nm has a QE peak of 22%.

Photoelectrons generated by Bi-alkali are focused at first dynodes. In an SKPMT, the collection efficiency at the first dynode is 70% on average, which is uniform within ±7%. At the dynode, a total voltage of 1500 to 2000 V is applied, and photoelec-

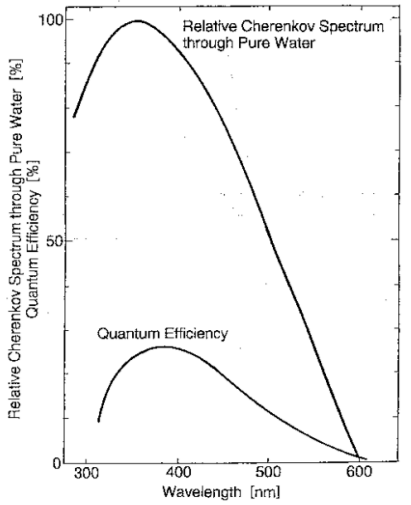

Figure 20: Quantum efficiency of an SKPMT and the wavelength spectrum of Cherenkov radiation in the water.

trons are amplified $\mathcal{O}(10^7)$ times. Therefore, an SKPMT is capable of detecting a single photoelectron. Table 2 illustrates the performance of an SKPMT. The time resolution of one photoelectron is 2.2 ns, and the dark noise rate is approximately 3 kHz at a 0.25 photoelectron threshold.

2.4.4 Data Acquisition System

The Data Acquisition System (DAQ) of the SK was updated in September 2008. Following this update, the SK data were referred to as SK-4. Because the data used in this thesis only include SK-4, its DAQ is discussed. Figure 21 presents a flowchart of the DAQ of SK-4. The SK-4 uses electronics called QTC-Based Electronics with Ethernet (QBEE) [21]. Figure 22 illustrates the QBEE board. The QTC is a high speed charge-to-time converter(IWATSU CLC 101) and it is an application-specific integrated circuit (ASIC). In addition, the QBEE is composed of a multi-hit Time-to-Digital Converter (TDC) and an FPGA, 1.5 MB FIFO memory, and an ethernet subboard.

Figure 23 presents a block of the QTC. The QTC has three channels with different gains: small, medium, and large. The gains are 1:7:49: thus, the dynamic range of the QTC is 0.2∼2500 pC, which is enough sufficiently wide range.

The QTC expresses the signal timing at the leading edge with respect to the input signal and outputs a short pulse whose width is the ratio of the charge. First, the signal input to the QTC is amplified by Low Noise AMP (LNA) and then divided into two signals for use in the discriminator and charge measurement. Thus, when the input signal exceeds the threshold, 0.25 p.e., the gate for the charge measurement

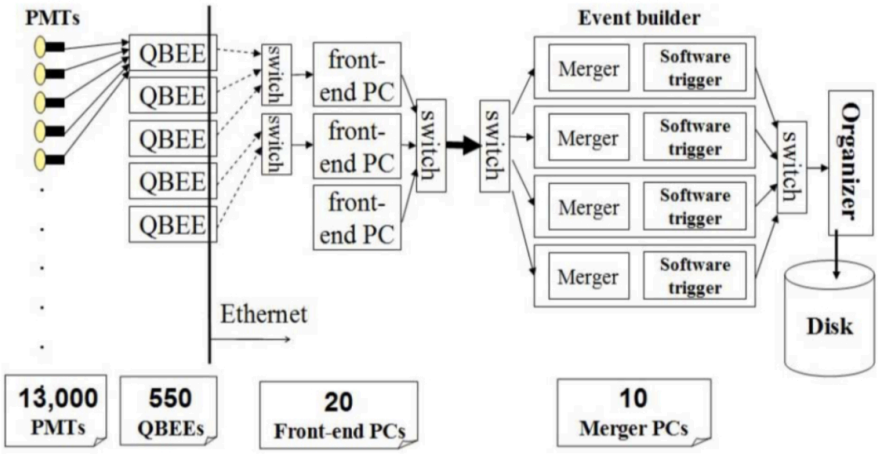

Figure 21: Diagram of the Super-Kamiokande data acquisition system (DAQ).

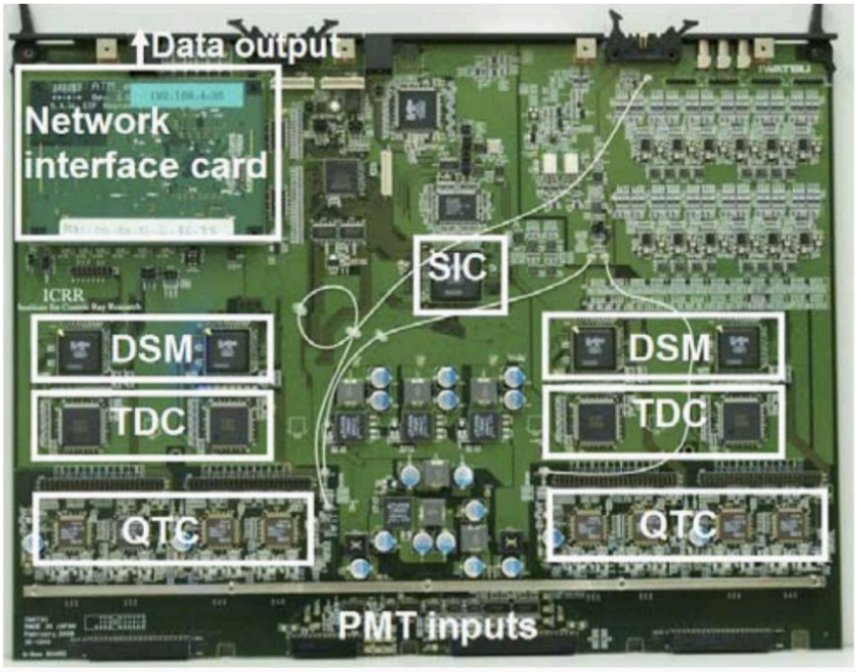

Figure 22: QBEE board for the Super-Kamiokande.

Table 2: Specifications of SKPMT (Hamamatsu R3600 PMT)

Photocathode area	50.8 cm diameter
Shape	Hemispherical
Window material	Pyrex glass (4 *sim* 5 mm)
Photocathode material	Bialkali (Sb-K-Cs)
Dynodes	11 stage Venetian blind type
Spectral Response	300 nm to 650 nm
Quantum efficiency	22 % at $\lambda = 390$ nm (peak)
Gain	10^7 at ~ 2000 V
Dark current	200 nA at 10^7 gain
Dark noise rate	3 kHz at 10^7 gain
Cathode non-uniformity	$< 10\%$
Anode non-uniformity	$< 40\%$
Transit time	90 ns at 10^7 gain
Transit time spread	2.2 ns RMS at 1 p.e. levels
Weight	13 kg
Pressure tolerance	6 kg/cm2 water pressure

a 400 ns window is opened and the charge is integrated. Figure 24 presents a timing chart of the QTC.

- GPS trigger to save the T2K event

In the SK, a GPS system is used for data synchronization with the T2K experiment. The SK DAQ system (sukonh02) receives and saves the GPS data from the T2K and the beam spill data from J-PARC, saving the GPS time. The SK DAQ system opens the T2K software trigger to save the beam data when the T2K experiment is completed. Figure 25 illustrates the gate timing and time windows. The T2K data are saved for all PMT hits between ± 500 μs after the beam arrival time. A time difference of approximately 1 ms is provided considering the Time of Flight (TOF) of a neutrino. T2K timing gate can be observed in the data because the total time for eight bunch spills of the T2K is within 5 μs. The SK uses two types of GPS: GPS1 and GPS2. By comparing the difference between the two, the accuracy of the GPS can be determined: the time difference between the two GPS system is less than 200 ns. As a result, the data error due to GPS errors in the current T2K-Run 1-4 is less than 0.05%.

2.4.5 SK-Gd

The SK-Gd project involves dissolving 0.1% mass concentration of gadolinium(Gd), 0.2%Gd(Gd2(SO4)3), in the Super-Kamiokande [22]. Gd has a very high neutron

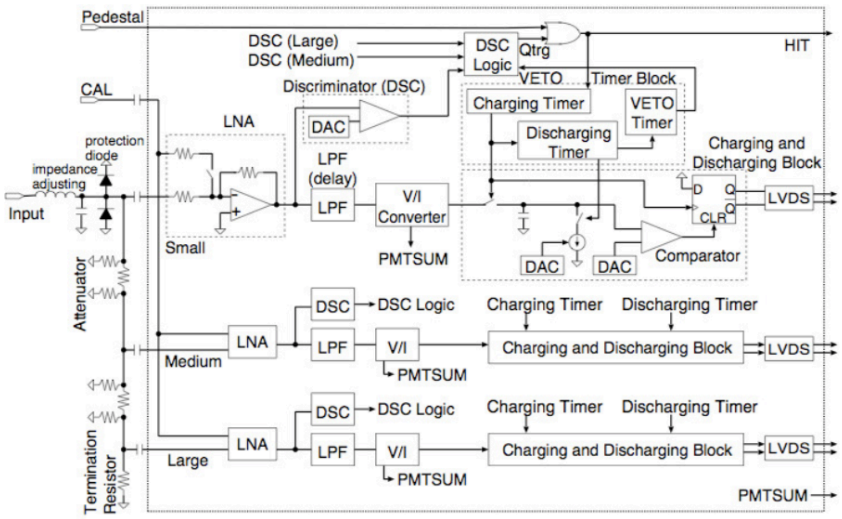

Figure 23: Block diagram of one QTC channel.

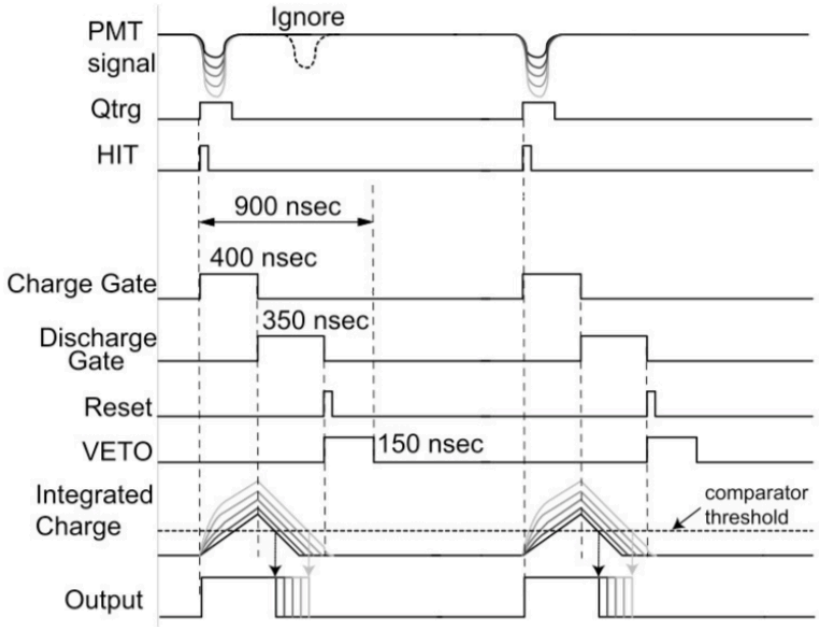

Figure 24: Timing chart for QTC operation.

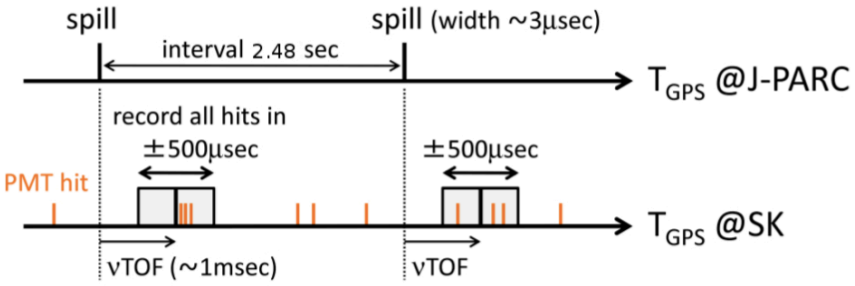

Figure 25: The T2K and Super-Kamiokande are synchronized by GPS in consideration of neutrino TOF. The recording time for one spill is 1 ms.

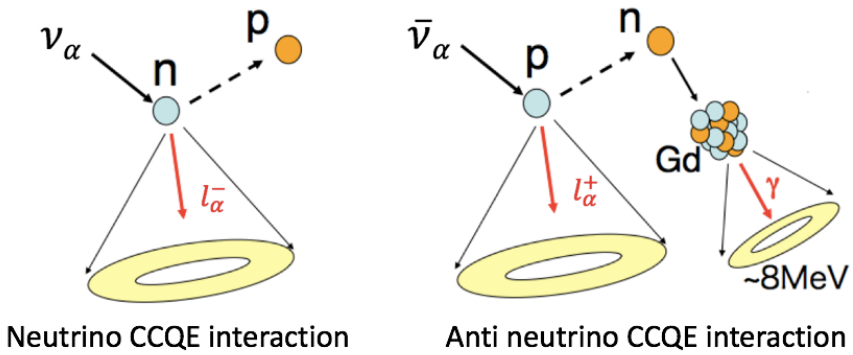

Figure 26: The left image illustrates the neutrino CCQE interaction, and the right image illustrates the anti neutrino CCQE interaction in the SK-Gd.

capture cross section (49,700 barn) and emits the total of 8 MeV gamma rays when capturing neutrons. Utilizing this property, the SK-Gd distinguishes between inverse beta decay signals and background, as shown below:

$$\overline{\nu}_e + p = e^+ + n \tag{18}$$

In the SK-Gd, an emitted neutron is captured by Gd, and total 8 MeV gamma rays are emitted. Figure 26 illustrates this interaction. For a 0.1% Gd concentration, the average capture time is 30 μs, and 90% of the neutrons are captured by the Gd nucleus. Figure 27 depicts the neutron capture efficiency as a function of Gd concentration.

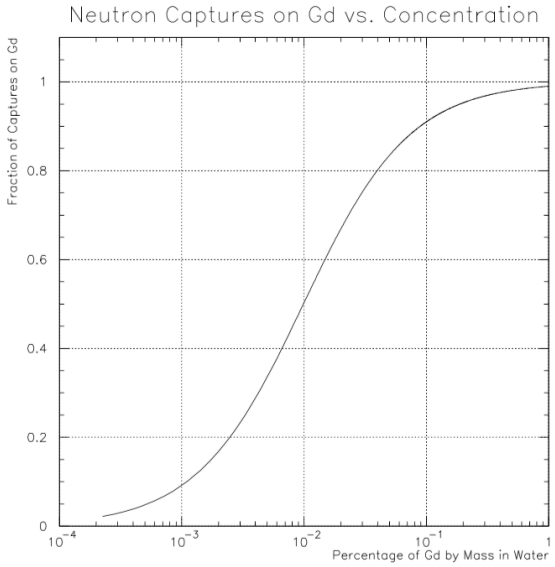

Figure 27: Neutron tagging efficiency as a function of Gd concentration. The horizontal axis represents the mass concentration [%] of Gd in water, and the vertical axis represents the thermal neutron capture efficiency by Gd.

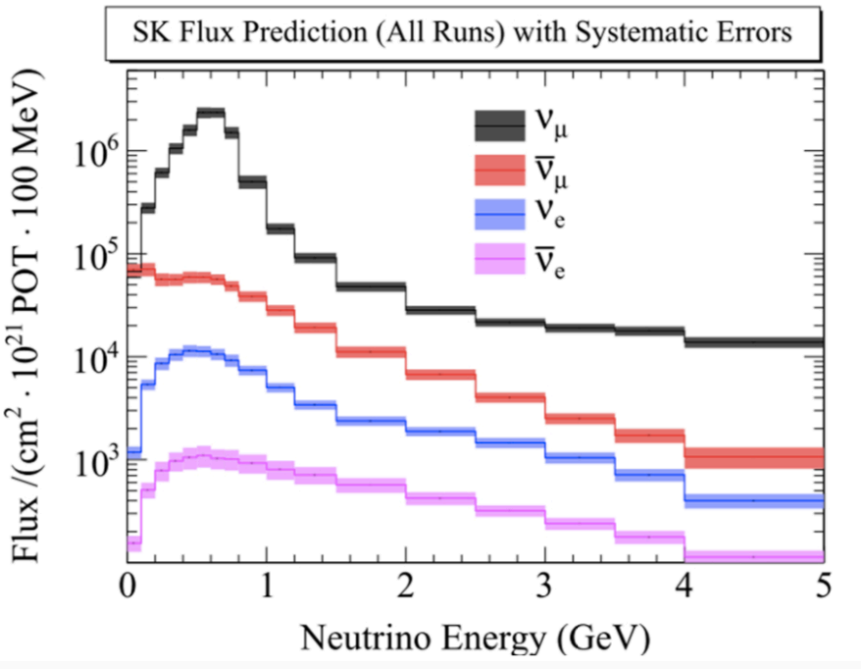

Figure 28: T2K neutrino beam flux in the SK [27]. The effect of neutrino oscillation is not considered. The width of each color represent the systematic error.

3 Simulation

A T2K NCQE event was simulated in three steps. First, the neutrino flux passing through the SK in T2K beam was simulated. Then, the neutrino-nucleus interaction was simulated. Finally, the interaction in the SK tank was simulated.

3.1 T2K neutrino beam simulation

A T2K neutrino beam flux was simulated using primary proton beam, target, neutrino beam alignment and off-axis angle. In this simulation, the interaction between graphite and 3-GeV protons was first calculated by the FLUKA [23], which calculates hadron interaction using experimental data from the CERN NA61/SHINE experiment [24], [25]. This experimental data covers most of the phase space relevant for the T2K.

The particles generated by this simulation are then used in a GEANT3 simulation [43], which simulates the decay of neutrinos from particles: this involves the secondary beam line. From the result, 2.5° off-axis T2K beam flux is simulated. Figure 28 illustrates the neutrino flux in the SK [27].

3.2 Neutrino interaction model

The interaction of a T2K beam neutrino and water in the SK is simulated by NEUT [28], a neutrino interaction simulation program library that can simulate interactions with various substances, such as oxygen, hydrogen, protons, carbon, and iron. The INGRID and ND280 detectors are also simulated using the NEUT. The final state interactions which are interactions within the nucleus, are simulated in the NEUT process. The following interactions can be simulated using NEUT:

- Neutral Current Quasi-Elastic Scattering: $\nu + X \rightarrow \nu + (X-1) + N'$
- Charged Current Quasi-Elastic Scattering: $\nu + n \rightarrow l^- + p$
- CCSingle π, K, η ResonanceProduction: $\nu + N \rightarrow l^- + N' + \pi(\eta, K)$
- NCSingle π, K, η ResonanceProduction: $\nu + N \rightarrow \nu + N' + \pi(\eta, K)$
- CC Coherent π productions: $\nu + X \rightarrow l^- + X + \pi$
- NC Coherent π productions: $\nu + X \rightarrow \nu + X + \pi$
- CC Deep Inelastic Scattering: $\nu + N \rightarrow l^- + N' + m\pi(\eta, K)$
- NC Deep Inelastic Scattering: $\nu + N \rightarrow \nu + N' + m\pi(\eta, K)$
- CC 2p2h Interaction : $\nu + N \rightarrow \nu + N' + m\pi(\eta, K)$

where, X is the target nucleus, N and N' are the target or outgoing nucleons, l is an outgoing charged lepton, and m is the number of created π. Figure 29 illustrates a neutrino-nucleon cross section in each interaction. NEUT simulates neutrino-nucleon interactions, the emission of de-excitation gamma rays, and emitted neutrons or protons in final state interactions.

3.2.1 NCQE interaction

The Llewellyn-Smith model is used as the basis for describing NCQE in NEUT. The current NCQE cross-section has been calculated by M. Ankowski and Omar Benha [29], and follows the procedures in [30] and [31] as follows:

$$\frac{d^2\sigma_\nu}{d\Omega dE'_\nu} = \frac{G_F^2 E'_\nu L_{\mu\nu} W^{\mu\nu}}{8\pi^2 E_\nu M E_{N'}} \delta(\tilde{\omega} + E_N - {E_N}') \tag{19}$$

where, E_ν is the momentum of the first neutrino, E'_ν is the output neutrino momentum, ${E'}_N = \sqrt{M^2 + \mathbf{p'}^2}$, G_F is the Fermi constant, M is the nucleon mass, and $\tilde{\omega}$ is the difference in momentum in a weak interaction. The lepton tensor $L_{\mu\nu}$ and hadronic tensor $W^{\mu\nu}$ are given by

$$L_{\mu\nu} = 2(k'_\mu k_\nu + k'_\nu k_\mu - g_{\mu\nu} k k' - i\epsilon_{\mu\nu\alpha\beta} k^\alpha {k'}^\beta) \tag{20}$$

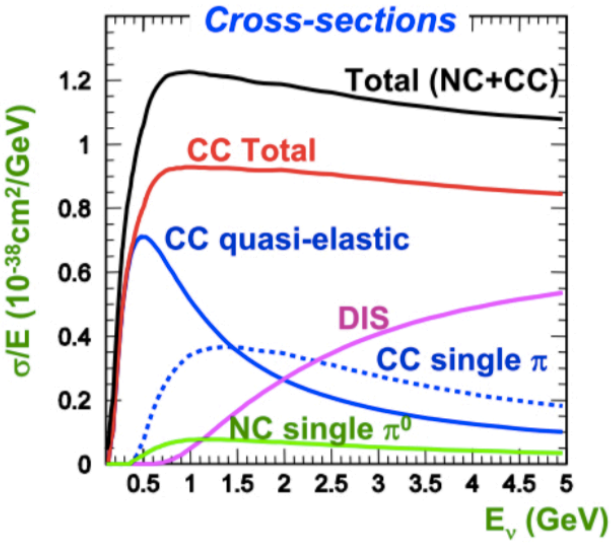

Figure 29: Neutrino-nucleus cross-sections in NEUT simulation

$$
\begin{aligned}
W^{\mu\nu} = &-g^{\mu\nu}M^2W_1 + \tilde{p}^{\mu}\tilde{p}^{\nu}W_2 + i\epsilon^{\mu\nu\alpha\beta}\tilde{p}_{\alpha}\tilde{q}_{\beta}W_3 \\
&+ \tilde{q}^{\mu}\tilde{q}^{\nu}W_4 + (\tilde{p}^{\mu}\tilde{q}^{\nu} + \tilde{p}^{\nu}\tilde{q}^{\mu})W_5
\end{aligned}
\tag{21}
$$

where W_j is the structure function written as follows:

$$
\begin{aligned}
W_1 &= \tau(F_1^N + F_2^N)^2 + (1+\tau)(F_A^N)^2 \\
W_2 &= (F_1^N)^2 + \tau(F_2^N)^2 + (F_A^N)^2 \\
W_3 &= (F_1^N + F_2^N)F_A^N \\
W_4 &= \frac{1}{4}[(F_1^N)^2 + \tau(F_2^N)^2 - (F_1^N + F_2^N)^2 - 4F_P(F_A^N - \tau F_P^N)] \\
W_5 &= \frac{1}{2}W_2
\end{aligned}
\tag{22}
$$

where $\tau = -\tilde{q}^2/4m_N^2$, F_j^N is a form factor that is written as

$$
\begin{aligned}
F_1^N &= \pm\frac{1}{2}F_1 - 2\sin^2\theta_W F_1^{EM,N} \\
F_2^N &= \pm\frac{1}{2}F_2 - 2\sin^2\theta_W F_2^{EM,N} \\
F_A^N &= \pm\frac{1}{2}(F_A^s \pm FA) = \frac{1}{2}\frac{\Delta s \pm g_A}{(1 - q^2/M_A^2)^2} \\
F_P^N &= \frac{2m_M^2 F_A^N}{m_\pi^2 - q^2}
\end{aligned}
\tag{23}
$$

where F_1^N is the Dirac from factor, F_2^N is the Pauli from factor and F_A^N is the axial vector nucleon weak neutral current form factor. θ_W is the mixing angle of the weak

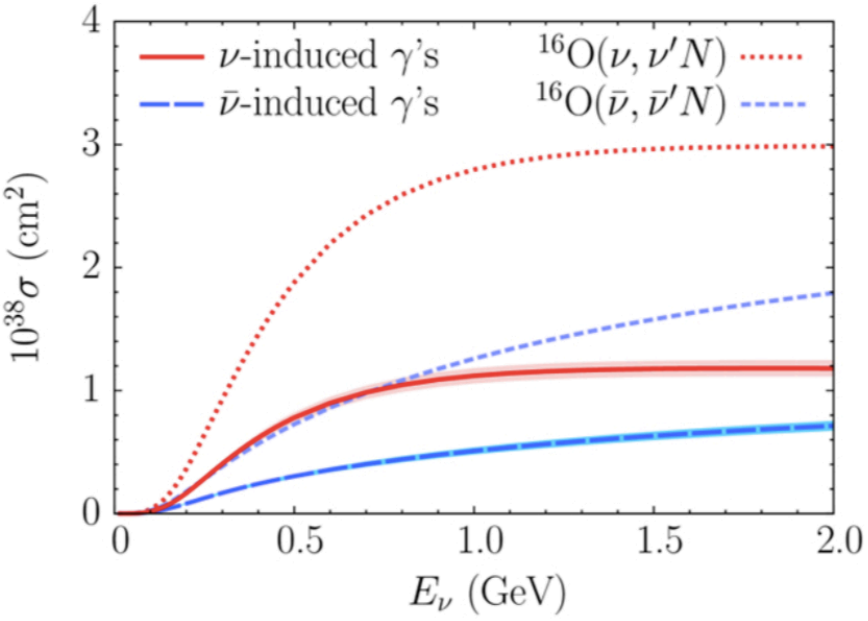

Figure 30: Theoretical ν NCQE cross-section used in this thesis, which is represented by the red dotted line. The blue short-dashed line represents the $\overline{\nu}$ NCQE cross-section, and the red solid line and blue long-dashed line represent the theoretical cross-section only emitted by gamma rays above 6 MeV [29].

interaction, N is a proton or neutron, $\Delta s = -0.08$ is the strange quark contribution, g_A is -1.2673, and m_π, is the mass of a pion. F_1^N and F_2^N can be defined for electric form factor G_E^N and magnetic form factor G_M^N as follows:

$$F_1^N = \frac{G_E^N + \tau G_M^N}{1+\tau}$$
$$F_2^N = \frac{G_M^N - G_E^N}{1+\tau} \tag{24}$$

where G_E^N and G_M^N are parameterizations in NEUT [32], [33].

Figure 30 presents the theoretical NCQE cross-section used in this thesis [29]. Figure 31 illustrates the difference between the NCQE corss-section and other NC cross-section. The NCQE cross-section is dominant in the T2K beam energy region of ∼630 MeV.

3.2.2 De-excitation gamma ray via NCQE interaction

This section, discusses de-excitation gamma rays via the NCQE interaction in the NEUT the main focus of this thesis. The Neutrino-Oxygen NCQE interaction knocks out a nucleon from an oxygen-nucleus. Then, the residual nucleus transfers to various

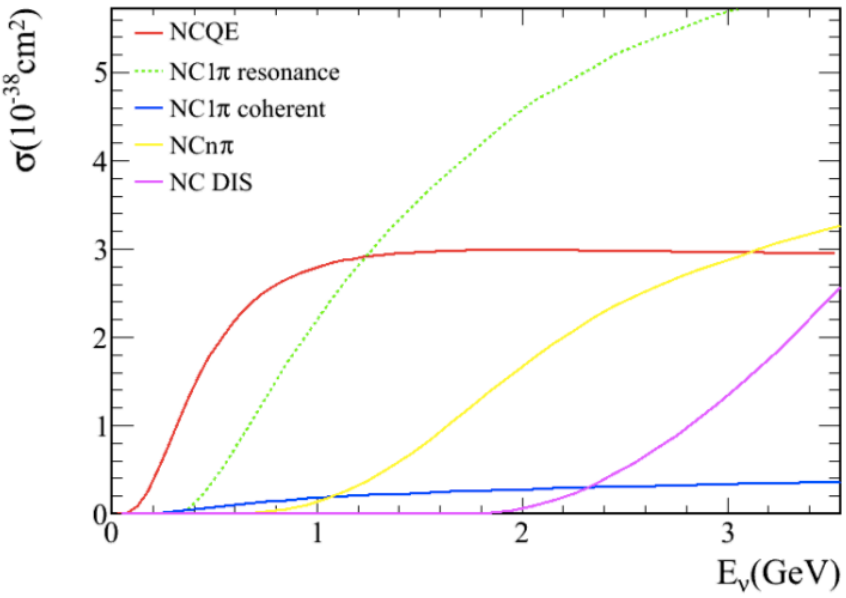

Figure 31: Comparison between neutral current interaction cross-section. At 630 MeV, the NCQE cross-section is dominant.[28]

excited states. Figure 32 illustrates the NCQE interaction, and a sample interaction is presented below.

- $\nu + {}^{16}O \rightarrow \nu + {}^{15}O^* + n$
- $\nu + {}^{16}N \rightarrow \nu + {}^{15}N^* + p$
- $\nu + {}^{16}O \rightarrow \nu + {}^{14}N^* + n + p$
- $\nu + {}^{16}O \rightarrow \nu + {}^{14}B^* + p + p \cdots$

The residual nucleus emits de-excitation gamma-rays with various energy levels. Among them, the NCQE interaction is mainly observed via gamma rays of approximately 6 MeV, as they can be observed in the SK. The de-excitation gamma-rays are referred to as primary gamma rays. Figure 2 presents a schematic of the de-excitation gamma rays via the NCQE interaction. In addition, it illustrates secondary gamma rays, which are described in more detail in Section 3.3.1.

- Spectral function and spectroscopic factor

The spectral function $P(\mathbf{p}, E)$ describes the probability of removing a nucleon $\phi(\mathbf{p})$ with momentum $\mathbf{p}$ from a nucleus with removal energy E. The spectral function of an oxygen nucleus is derived using the local density approximation(LDA),

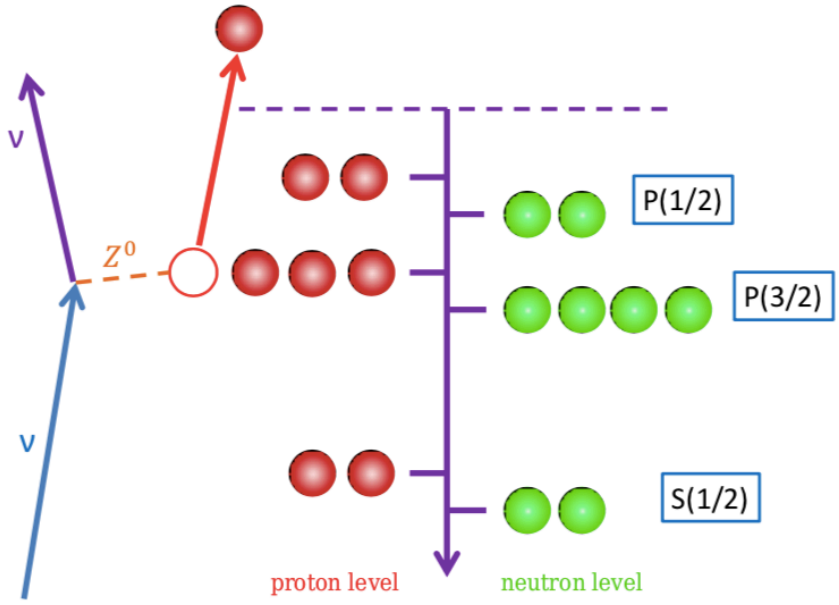

Figure 32: Diagram of de-excitation gamma rays via NCQE interaction. Here, the proton at the p3/2 state is knocked out.

which combines theoretical calculations for nuclear and electron scattering experimental data [34], [35]. The LDA spectral function of ^{16}O is obtained through the combination of experimental data regarding nucleon removal and theoretical calculations of the nuclear at different densities. The spectral function of an oxygen nucleus is presented in Figure 33 using the LDA.

The probability of removal from an oxygen nucleus is dependent on the removal energy, E. The removal energies of oxygen are 12.1, 18.4, and 42 MeV in a simple shell model. In the LDA, the knockout energy is not a single value for each nucleon state. Figure 34 depicts the removal energy distribution, which is calculated by the integral of the spectral function. The left peak is the $p_{1/2}$ state, the right peak is the $p_{2/3}$ state, and $s_{1/2}$ is distributed over a wide range.

The spectroscopic factors are then calculated by the integration of each energy range and are summarized in Table 3.

Table 3: Spectroscopic factor of each nucleon state in oxygen.

Residual nucleus	$p_{1/2}$	$p_{2/3}$	$s_{1/2}$	Others
^{15}N	0.188	0.3515	0.1055	0.385
^{15}O	0.188	0.3515	0.1055	0.385

- Branching ratio of primary gamma-rays

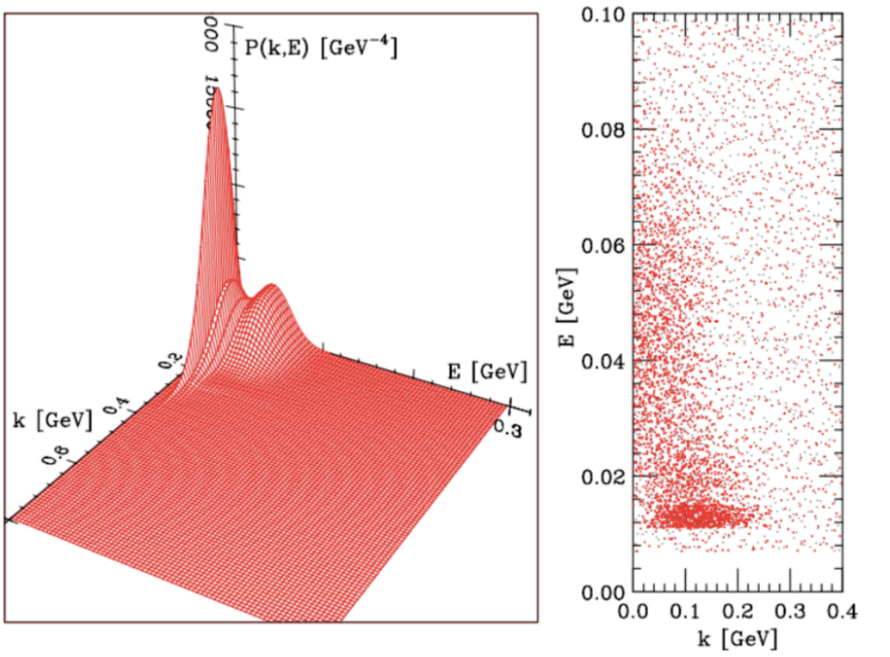

Figure 33: Spectral function of an oxygen nucleus using an LDA-based calculation. On the left plot is a three dimensional plot of a spectral function, and on the right is a scatterplot [30].

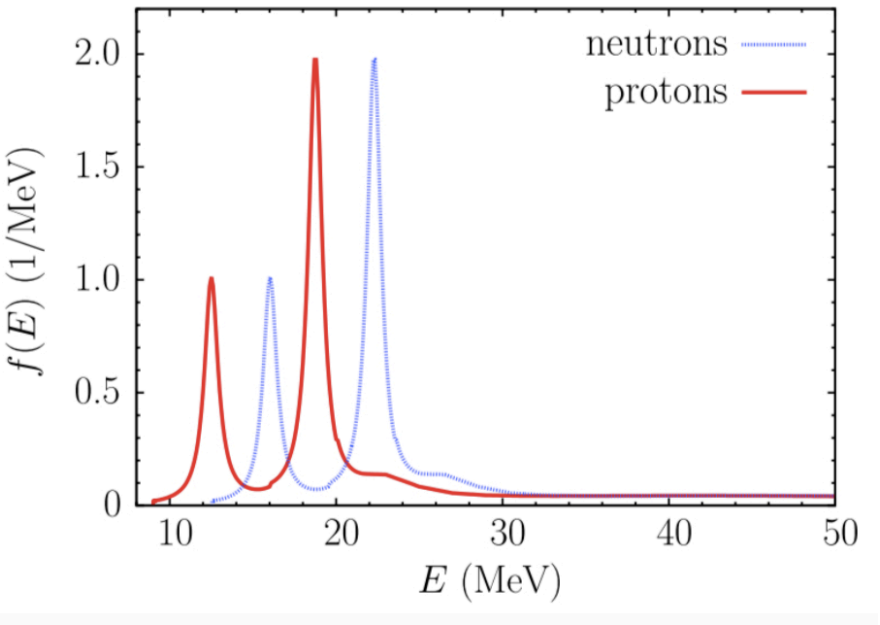

Figure 34: Removal energy distribution from the integration of the spectral function. The neutrons are bound more strongly (by 3.54 MeV) to the nucleus than the protons [29].

The branching ratio of the primary gamma-rays is described for each energy state, $p_{1/2}$, $p_{3/2}$, and $s_{1/2}$ and the others state.

- $p_{1/2}$ state

Generally, gamma rays do not occur in this state.

- $p_{3/2}$ state

This state releases gamma rays above 6 MeV with the highest probability. The branching ratio is summarized in Table 4[37]. This probability is provided by the $^{16}O(e, e'p)^{15}N$ experiment in NIKHEF-K[38] and others [39].

- $s_{1/2}$ state

When the $s_{1/2}$ state returns to the ground state, it emits several nucleons. The branching ratio is summarized in Table 5 [40]. This ratio is obtained from the E148 experimental results from the Research Center for Nuclear Physics (RCNP) [41], [42].

- Others state

Table 4: Summay of the energy levels and gamma-ray emission branching ratios for the $p_{3/2}$ nucleon hole state.

Residual isotope	Energy level (MeV)	E_γ (MeV)	E_p (MeV)	Ratio of E.L(%)	BR in E.L(%)	Final BR $\gamma + Y$(%)
^{15}N	6.32	6.32	-	86.9	100	86.9
	9.93	9.93	-		77.6±1.9	3.8
		5.27+5.30	-	4.9	15.4±1.5	0.8
		6.32	-		4.9±1.2	0.24
		7.30	-		2.1±0.8	0.1
	10.70	-	0.5	8.2	-	-
^{15}O	6.18	6.18	-	86.9	100	86.9
	9.61	-	0.5	4.9	-	-
	10.48	-	0.5	8.2	-	-

The removal energy of ^{16}O above 62 MeV is referred to as continuum nucleon states, which are extended up to 300 MeV. However, there are no quantitative results on gamma emission from these state. Thus, the continuum nucleon states in this simulation do not emit gamma rays.

- Summary of primary gamma-rays energy distribution

The distribution of emitted gamma rays from all states is presented in Figure35. In the NCQE interaction, gamma ryas of approximately 6 MeV are dominant.

3.3 Super-Kamiokande simulation

The final state interaction was simulated using NEUT. In this section, the simulation of the interaction in the SK is discussed.

An Super-Kamiokande detector simulation(SKDETSIM) is a detector simulation that reproduces SK based on GEANT3(v 3.21) [43]. SKDETSIM emitted nucleons, Cherenkov light due to charged particles in water, photon absorption and scattering, and the photon detection probability by the PMTs.

3.3.1 Secondary gamma simulation

In this section, secondary gamma-rays from the NCQE interaction are discussed. The NCQE interactions emit protons or neutrons. Figure 36 illustrates the neutron and proton energy distribution by the NCQE interaction in the NEUT simulation. Proton is quickly stopped by ionization loss; by contrast, neutrons do not cause ionization loss. Thus, neutrons collide with other nuclei, such as an oxygen or hydrogen

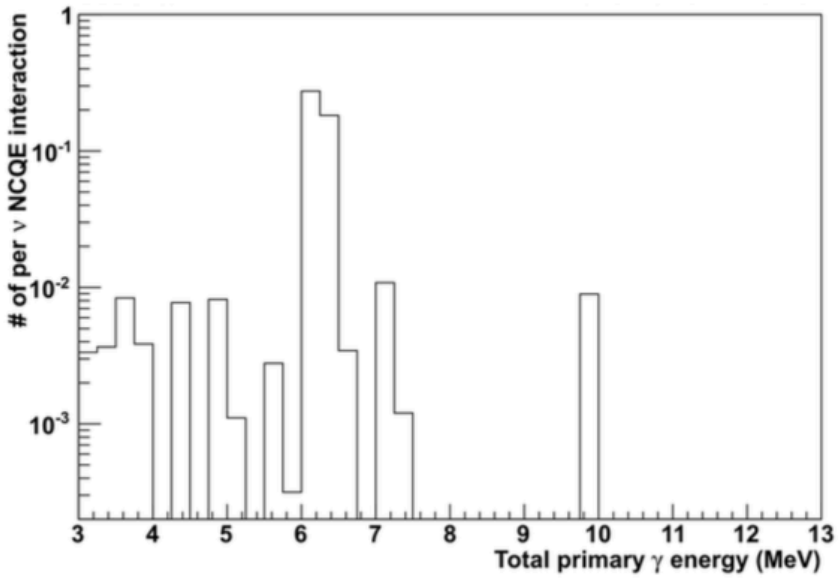

Figure 35: Primary gamma-ray energy distribution. Gamma rays of approximately 6 MeV dominate.

nuclei. When they collide with oxygen nuclei, they often emit de-excitation gamma-rays called secondary gamma-rays. Several 10 MeV to approximately 1,000 MeV neutrons are emitted. Figure 38 displays the energy distribution of the secondary gamma rays in the current simulation.

The SKDETSIM can simulate Cherenkov light and charged particles with high accuracy via calibration and external experiment. However, the secondary gamma-ray simulation in the SKDETSIM currently faces challenges because there are no experimental data, on the interaction between neutrons of several 10 MeV to 1,000 MeV and water. Currently, the SKDETSIM uses the GCALOR[44] of GEANT3.

In GCALOR, hadron interaction are simulated by MICAP [55] in $E_N < 20$ MeV. However, NMTC [46] is used for 20 MeV $< E_N <$ 3500 MeV. Figure 37 presents the gamma-ray distribution from the NCQE interaction using the current model. The model boundary of 20 MeV demonstrates a difference; therefore, there is a large uncertainty.

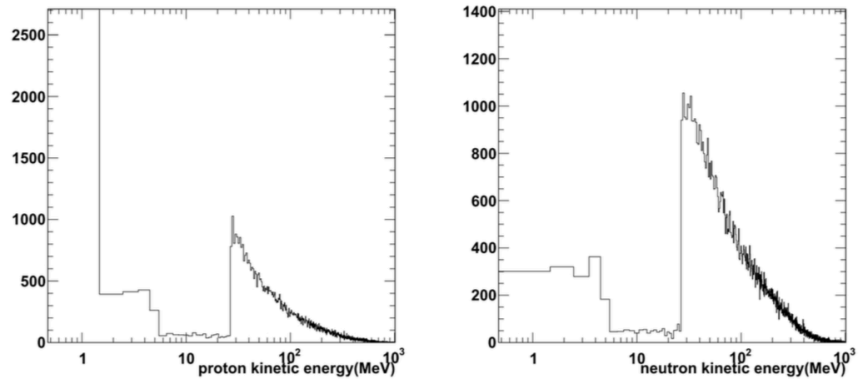

Figure 36: Expected the proton and neutron energy distribution from the T2K NCQE interaction. The left plot represents proton energy, and the right plot represents neutron energy.

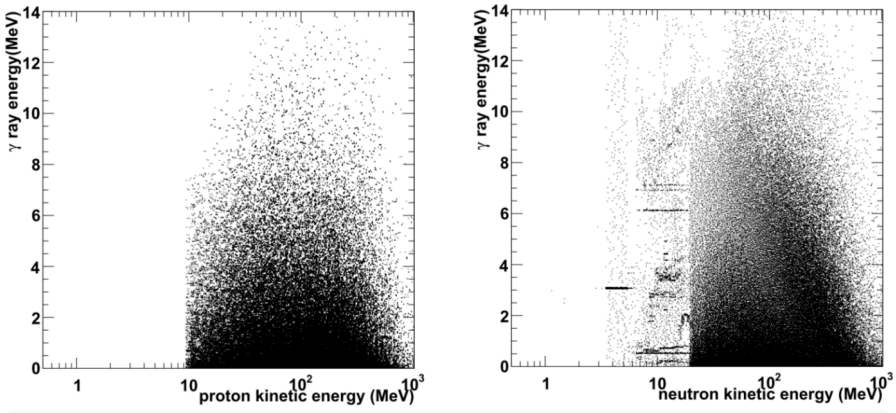

Figure 37: Secondary gamma ray energy distribution depends protons and neutrons. The left plot illustrates the proton vs. de-excitation gamma ray distribution, and the right figure illustrates the neutron vs. de-excitation gamma ray distribution.

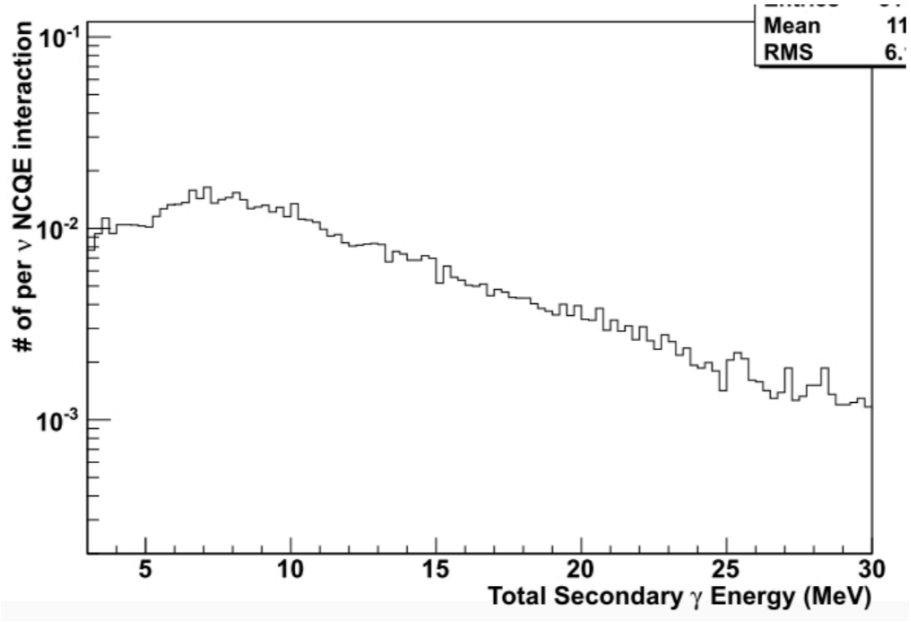

Figure 38: Secondary-gamma ray energy distribution from the NCQE interaction.

Table 5: Summaries of the energy levels and the gamma-ray emission branching ratios for the $s_{1/2}$ nucleon hole state.

Residual isotope	Energy level (MeV)	E_γ (MeV)	BR in E.L(%)	Final BR $\gamma + Y$(%)
^{13}C+d	3.09	3.09	100	3.0
	3.68	3.68	99.3	4.2
	3.85	3.09	1.20	4.6
		3.68	36.3	
		3.85	62.5	
^{12}C+t	4.44	4.44	100	5.8
^{14}N+n	4.92	4.92	97	5.2
	5.11	5.11	79.9	¡0.1
	5.69	3.38	63.9	4.5
		5.69	36.1	
	5.83	5.11	62.9	0.54
		5.83	21.3	
	6.20	3.89	76.9	¡0.1
		6.20	23.1	
	6.45	5.11	8.1	2.8
		6.45	70.1	
	7.03	7.03	98.6	(6.7)
^{14}C+p	6.09	6.09	100	(¡0.1)
	6.59	6.09	98.9	(¡0.1)
	6.73	6.09	3.6	(0.43)
		6.73	96.4	
	6.90	6.09	100	(¡0.1)
		6.09	1.4	(6.7)
	7.01	7.01	98.6	
	7.34	6.09	49.0	5.7
		6.73	34.4	
		7.34	16.7	

4 Event selection and data analysis

In this section, event selection of NCQE gamma rays from the T2K data is described. Monte Carlo(MC) simulation uses nearly the same selection.

4.1 NCQE Event selection

Several selection conditions are applied in searching for NCQE gamma events in the T2K data. Table 6 summarizes the selection conditions.

Table 6: Summary of event selection terms

Selection type	Contents
T2K good beam spill	good ν beam and good SK data
Reconstruction energy	4 MeV $\leq E_{rec} \leq$ 30 MeV
Timing	ΔT_0 within 100 ns $\pm$ from bunch centers
Fiducial Volume	vertex point to ID 2m
DWall	vertex point to ID
EffWall	vertex point to ID
OvaQ	reconstruction quality
Pre-activity	Beam unrelated event
Cherenkov angle	θ_{rec} >34.0°

4.1.1 T2K beam data

In this thesis, T2K Run1 to 4 from January 2010 to May 2013 are analyzed. These data are only neutrino mode (ν_μ beam), and the sum of the Proton on Target(POT) are 6.57 $\times 10^{20}$ POT. Table 7 summarizes the POT of each Runs.

Table 7: Summary of data from T2K Run1-4.

T2K Run	♯ of good spill	Number of bunch	Good number of POT
T2K Run1	1.00×10^6	6	3.24×10^{19}
T2K Run2	1.480×10^6	8	11.09×10^{19}
T2K Run3	1.762×10^6	8	15.79×10^{19}
T2K Run4	3.306×10^6	8	35.61×10^{19}
Total	7.551×10^6		65.73×10^{19}

4.1.2 Good spill selection

All information on the T2K beam is sent from J-PARC to the SK-DAQ system [47]. The SK and T2K are synchronized within $\mathcal{O}(10)$ ns through GPS, thus, information on the hit PMTs within $\pm$500 μ s from the beam arrival time is recorded in the

SK-DAQ. Good neutrino beam data at J-PARC, in which there are no errors within a spill, result in setting a flag called *good beam spill*. In addition, data with a sufficiently high quality in the SK also result in setting a flag called *SK data quality*, which is defined as follows.

- SK DAQ alive: This reflects whether the SK DAQ system is running or not. The dead-time from Run1 to Run4 by this cut is 0.01%.
- Bad subrun cut: In the SK, sub-runs are recorded in SK data approximately every minute. In the SK, the DAQ system evaluates each sub-run as good or bad. The main cause for a bad flag is the flasher noise of PMTs and SK DAQ difficulties. The dead-time of the data from Run1 to 4 by this cut is approximately 0.31%.
- GPS error: The T2K and SK must be synchronized using GPS. If there are problems synchronizing the GPS data, the T2K data is not analyzed. However, this error does not occur in Run1 to 4.
- Special data block: The SK electronics system records all PMT hit signals in a data block with a width of 16.7 μs. There are two types of special data blocks. The first block is a pedestal block, designed to store the pedestal data of all channels of the front end electronics. The second block is the TDC reset block, which resets the count of a part of the TDC chips. The dead-time of the data from Run1 to 4 by this cut is approximately 0.08%.

4.1.3 Energy cut

The energy cut of the NCQE de-excitation gamma rays in this analysis is 4 MeV $<$ Reconstruction energy $<$ 30 MeV [48], [49]. The 4 MeV trigger efficiency in the SK is greater than 99.5 %, and at above 30 MeV, there is Michel electron background from muons.

4.1.4 Timing cut

The NCQE gamma-ray data are cut by more detailed timing information. The event of -2 μs $<$ δ T_0 $<$ 10 μs is selected as T2K data on-timing using GPS time. There are a 8 bunch structures in the T2K data, and data pertaining only to this bunch timing in the GPS. Figure 43 presents the timing distribution of the neutrino events of the $\mathcal{O}$ (100 MeV) energy region observed by the SK and the timing distribution of the T2K beam spill. The $\mathcal{O}$ (100 MeV) energy region is displayed because there is a greater amount of statistics. As demonstrated in the Figure 43, 99% of the events are observed within 100 ns in RUN1 and RUN2. Therefore, the NCQE gamma event is analyzed within 100 ns.

4.1.5 Reconstruct vertex position cut

Radioactive impurities contained in the PMT materials and SK structure are one of the causes of background events that are not related to the beam. Therefore, background events are frequently occurring phenomenon near the ID wall. To reduce the background event rate, the reconstructed vertex events within 2 m of the ID wall are deleted.

To delete the background event entering FV from the ID wall, two parameters are used: dwall and effwall. First, dwall is defined as the distance from the reconstructed vertex to the closest ID wall. Second, effwall is calculated as the distance from the reconstructed vertex to the ID wall along the reconstruction direction. Figure 40 illustrates the FV, dwall and effwall instructions. Because dWall and effwall cuts have stricter criteria than FV volume cuts, the dWall and effwall thresholds are not shorter than 2 m for events with vertices inside the FV. Event with a dwall or effwall value shorter than the corresponding threshold are deleted; most of the deleted events are background from the inner wall of the detector.

4.1.6 Reconstructed quality cut

Upon rejecting the remaining background, the fit quality cut, ovaQ, is evaluated. The ovaQ is calculated by subtracting square of goodness of fit of the timing distribution for each hit PMT, G_V, and the square of goodness of the angle distribution for each hit PMT.

In SK, the reconstructed timing distribution of hit PMTs in neutrino events is generally narrow. By contrast, the timing distribution of background radiation is wide. The goodness vertex reconstruction distribution G_V is calculated using all hit PMT timing values as follows:

$$G_V = \frac{\Sigma e^{-\frac{1}{2}\frac{(\tau_i(\nu)-t_0)}{\omega}+\frac{(\tau_i(\nu)-t_0)^2}{\sigma}}}{\Sigma e^{-\frac{1}{2}\frac{(\tau_i(\nu)-t_0)}{\omega}^2}} \tag{25}$$

$$\tau_i(\nu) = t_i - \frac{|\nu - h_u|}{c} \tag{26}$$

where $\tau_i(\nu)$ is the TOF subtracted hit time, and t_0 is the fitted peak timing of the τ distribution. The sums are over all hits; this implies that, of the hit PMTs are narrowly distributed the value of G_V increases. Therefore, a small value of G_V indicates that the hit PMTs are broadly distributed.

In a neutrino event, the hit PMTs tend to be evenly distributed in the Cherenkov angular direction. The goodness of fit of the azimuth angle of a hit PMT is defined as follows:

$$G_A = t_i - \frac{max\{\angle_{uniform}(i) - \angle_{Data}(i)\} - min\{\angle_{uniform}(i) - \angle_{Data}(i)\}}{2\pi} \tag{27}$$

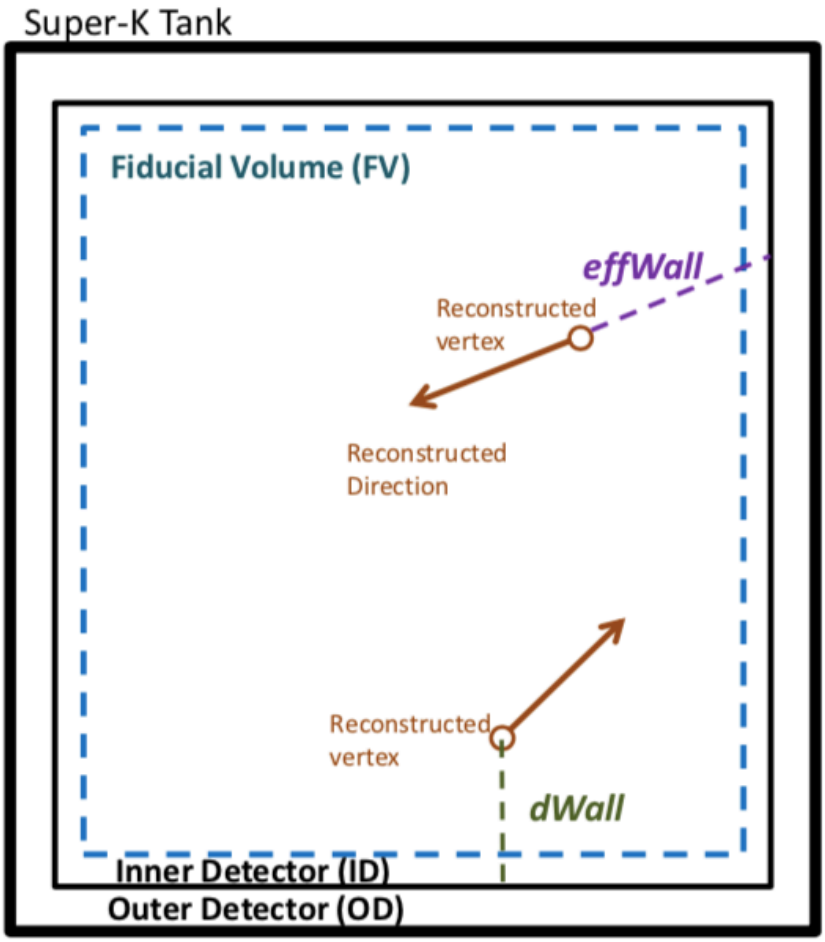

Figure 39: Diagram of the FV, effwall, and dwall. FV is located 2 m inside the ID wall. The effwall is the distance from the reconstructed vertex along the ID wall, and the dwall is the closest wall distance from the reconstructed vertex. The thresholds of dwall and effwall are depend on the energy.

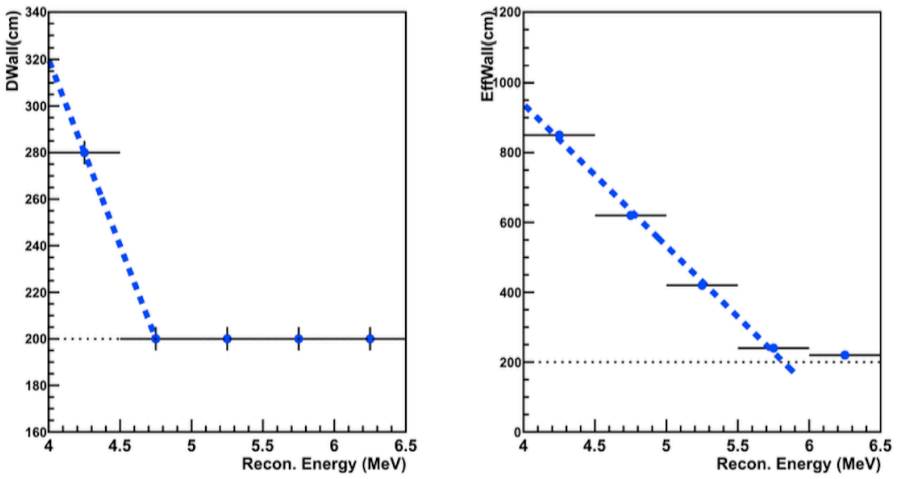

Figure 40: Thresholds of the effwall and dwall. Events under the blue line are rejected.

where $\angle_{uniform}(i)$ is the azimuth angle of the i-th hit PMT, assuming that the hit PMTs are uniformly distributed along with a Cherenkov cone. $\angle_{Data}(i)$ is the azimuth angle of a real data event. Therefore, a small value of G_A indicates that the hit PMTs are distributed uniformly.

Therefore, for information reconstructed by neutrino events, G_V is large, and G_A is small. Consequently, the events resulting from the goodness of the event reconstruction $ovaQ = G_V^2 - G_A^2$ are rejected when they are under a certain threshold. Figure 41 presents the thresholds of the cuts.

4.1.7 Pre activity cut

The background of the other unrelated beams involves ν_μ Charged Current (CC) interactions with low momentum cosmic muons and others. Low momentum muons emit very little Cherenkov light. These heavily charged particles then decay in the SK tank and emit decay electron; the background resulting from these electrons must be rejected. Low momentum muons are searched for in the 0.2 to 20 μs range prior to the candidates of NCQE gamma events. If the total number of hits within 30 ns exceeds 22, hits, the event is deemed a low energy muon event. The dead-time of the data from Run1 to 4 by this cut is approximately 0.1%.

4.1.8 Cherenkov angle cut

In addition, there is a background resulting from the neutrino beam that is caused by the generation of low momentum muons and pions by CC, NC, and NC others interactions. The almost neutrino beam signal emits the 42° Cherenkov light, as the muons have a sufficiently high momentum. However, muons with a momentum

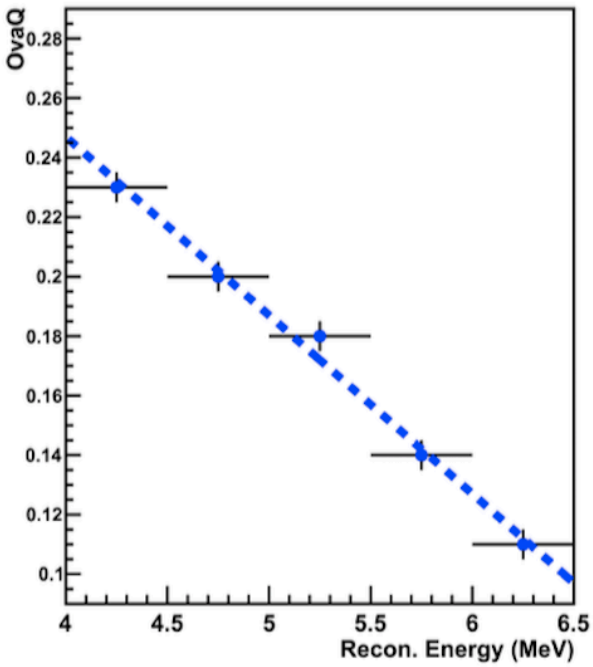

Figure 41: OvaQ threshold. Values under of blue line are rejected.

less than 250 MeV/c are slower than the speed of light in water. Therefore, the Cherenkov angle becomes smaller than 42°. The distribution of the peak angles is 28°. Therefore, events less than 34° are deleted. Figure 42 illustrates the Cherenkov angle distribution in each interaction.

4.2 Efficiency of NCQE reduction processes

Some NCQE interaction events are erroneously deleted as a background by the above mentioned selection processes. The selection efficiency is calculated via MC simulation and defined as the ratio of the number of all NCQE interaction signals greater than 4 MeV and less than 30 MeV to the number of NCQE interaction signals after all selections. The result indicate that the NCQE gamma detection efficiency is 83.9 % using these selections.

4.3 Result of NCQE event reduction

A total of 102 NCQE events were observed in the T2K Run1 to 4 data. The MC simulation estimated 100.2 events, including 72.2 NCQE events and 27 background events. Figures 45, 44, 45, 46, 47, and 48 display the energy, Cherenkov angle, dwall, effwall, and ovaQ distribution. These results are discussed in Section 6.

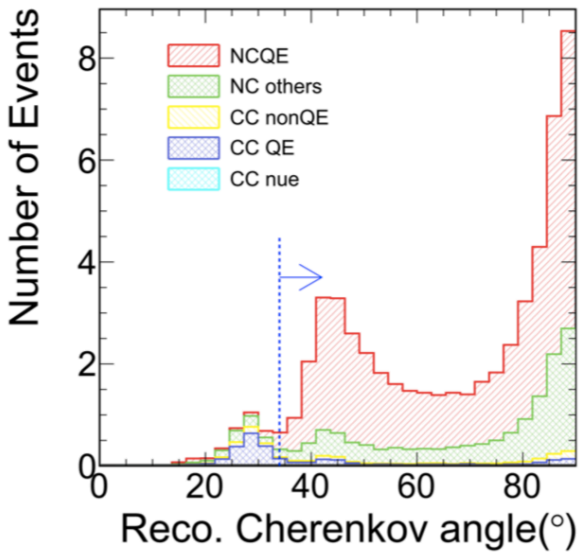

Figure 42: Cherenkov angle distribution for the T2K Run1-3 MC results. When the Cherenkov angle is smaller than 34°, the background event caused by the CCQE becomes dominant [12].

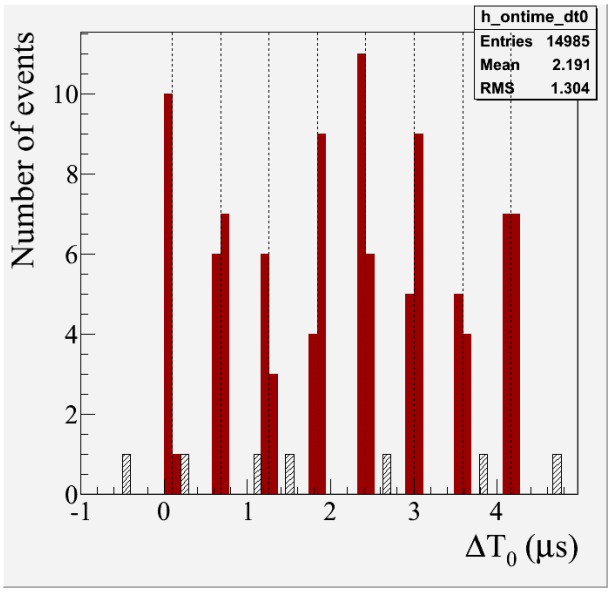

Figure 43: NCQE timing distribution. The on-timing and off-timing events are shown in solid and hashed.

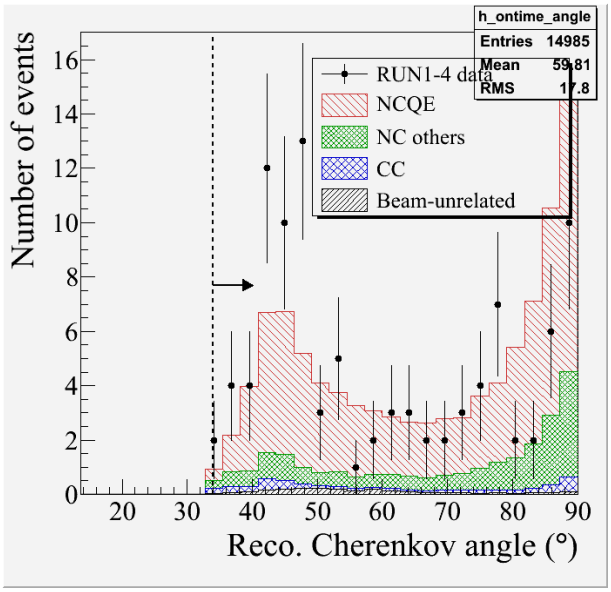

Figure 44: Reconstructed energy distribution of the data and MC. Black dots represent the data, and the histogram represents the MC results.

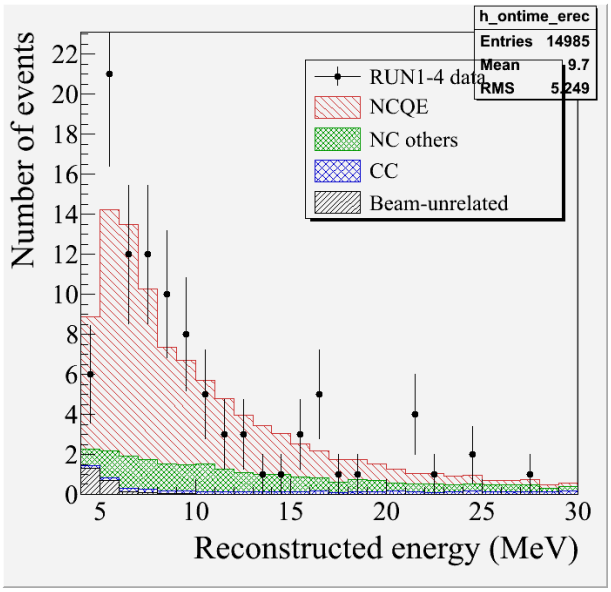

Figure 45: Cherenkov angle distribution of the data and MC results. Black dots represent the data, and the histogram represents the MC results.

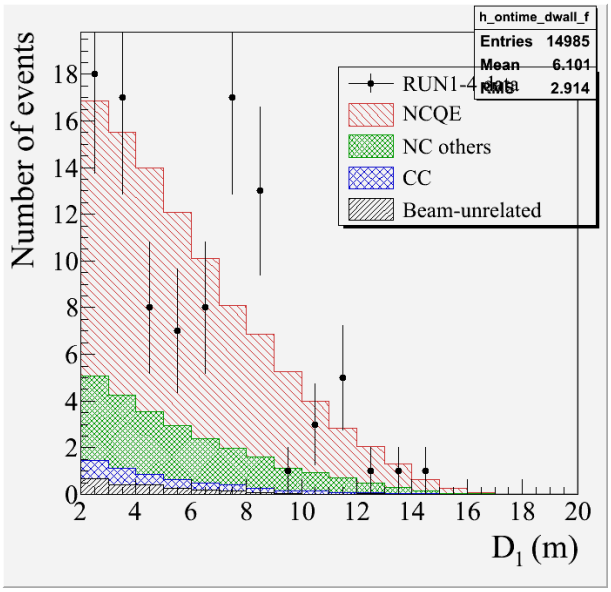

Figure 46: The dwall distribution of the data and MC results. Black dots represent the data, and the histogram represents the MC results.

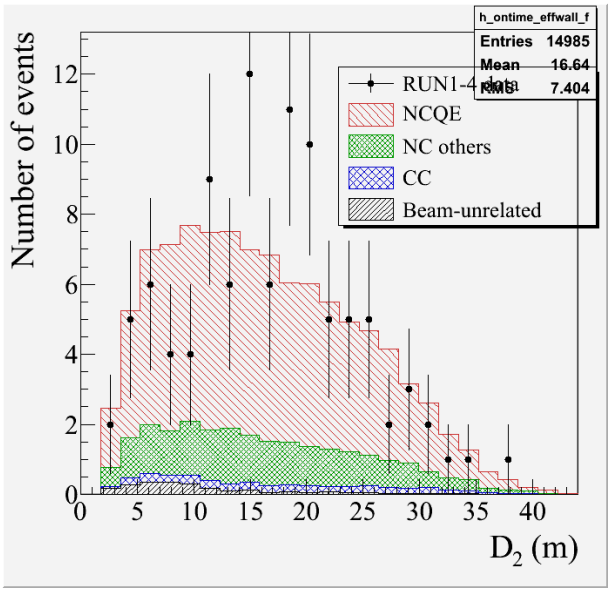

Figure 47: The effwall distribution of the data and MC results. Black dots represent the data, and the histogram represents the MC results.

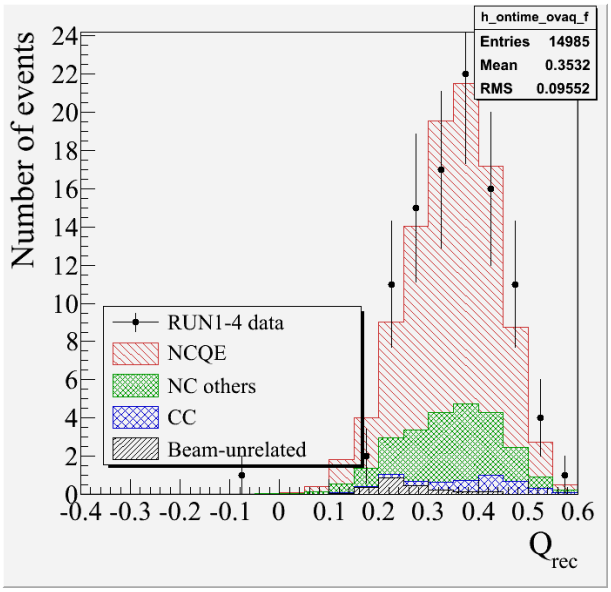

Figure 48: The ovaQ(goodness of reconstruction) distribution of the data and MC results. Black dots represent the data, and the histogram represents the MC results.

5 Systematic uncertainties

In this section, the systematic uncertainties of the NCQE gamma cross-section are discussed. The NCQE gamma cross-section measurements in this thesis have seven types of systematic uncertainties: Neutrino flux, Neutrino Interaction, Primary gamma, Secondary gamma, Super-Kamiokande detector, Oscillation parameter, Beam-unrelated uncertainties. Each uncertainties has an individual error parameter. The final NCQE gamma cross-section uncertainty is calculated by the multiplication of each systematic parameter by a Toy Monte Carlo (ToyMC) [50].

5.1 Neutrino flux and cross-section

In this subsection, T2K neutrino beam flux uncertainty is discussed. This uncertainty originates primarily from the hadron interactions models.

The T2K neutrino beam is simulated based on experimental results from the CERN NA61/SHINE hadron interaction experiment described in Section 3.1. Therefore, the uncertainty result from each parameter of the cross-section models of hadron production.

The uncertainty is calculated through a comparison between simulation and experimental result, which include T2K near detector measurement result and results from external experiment, MiniBooNE, SciBooNE, and NOMAD [51].

The cross-section and flux uncertainties are provided in Table 8.

Table 8: Cross-section and flux uncertainties.

Interaction	Flux	Cross-section
NCQE	11%	–
NC others	10%	18%
CC	12%	24%

5.2 Primary gamma

In this subsection, primary gamma emission model uncertainty is discussed. The uncertainty result from poorly understood gamma emission rates and spectroscopic factors of a nucleon removed from an oxygen nucleus, which is described in Section 3.2.2 [54]. The uncertainty is calculated through a comparison between a local density model and a simple shell model. In the NCQE interaction, $^{15}N^*$ or $^{15}O^*$ is the primary gamma emission. An excited nucleus has an excited state, and the single hole states are $p_{1/2}$, $p_{3/2}$ and $s_{1/2}$; in addition, there is continuum hole state. The $p_{1/2}$ state does not need to be considered because it does not emit gamma rays, and the remaining states are considered for gamma rays greater than 3 MeV, as low energy gamma rays are not observed in the SK. Table 9 is presents a summary of the uncertainties, and each state is summarized below.

Source	Uncertainty (%)
$p_{3/2}$	3
$s_{1/2}$	1
continuum states	3
multi-holes	9
Eγ < 3 MeV	1
Total	10

Table 9: Summary of the uncertainties of each primary-gamma source.

- $p_{3/2}$ hole state

The $p_{3/2}$ state emits gamma-rays with the highest probability in an NCQE interaction. There are four states in $p_{3/2}$: 9.93 NeV, 5.27 MeV +5.30 MeV, 6.32 MeV, and 7.30 MeV. The branching ratio and error of each states are given state is provided by the $^{16}O(e, ep)^{15}N$ experiment [52]. When the errors are maximally shifted, the NCQE-gamma event rate changes by 3%; therefore, the uncertainty of the p3/2 state is set to 3%.

- $s_{1/2}$ hole state

There are many gamma-ray emission processes in the $s_{1/2}$ state. The $^{16}O(p, p'p)^{15}N$ experiment in the E148 study provides the branching ratio. On the $s_{1/2}$ state, the emission probability of gamma rays above 6 MeV is $15.6 \pm 1.3^{+0.6}_{-1.0}$% and the emission probability for gamma rays between 3 MeV to 6 MeV are $27.9 \pm 1.5^{+3.4}_{-2.6}$% [54]. When the $s_{1/2}$ errors are maximally shifted, the NCQE-gamma event rate changes by 1%; therefore, the uncertainty of the $p_{3/2}$ state are set at 1%.

- States higher than $s_{1/2}$ state

States above the $s_{1/2}$ state are continuum hole states. There are no theoretical or experimental results regarding these states; thus, in our simulation, no gamma-rays in states above the $s_{1/2}$ state are emitted. However, the probability of deviation to this state is not high. Therefore, the simulation assumes that states above the $s_{1/2}$ state emit gamma rays identically to the $s_{1/2}$ state. In the results, the NCQE-gamma event rate changes by 3%; therefore, the uncertainty of the $p_{3/2}$ state is set to 3%.

- Gamma-rays below 3 MeV

Gamma-rays below 3 MeV are not simulated because there are no experimental data on the gamma-ray branching ratio. Therefore, the NEUT does not perform simulations of gamma-rays below 3 MeV. In principle, the SK cannot readily observe

below gamma rays below the 3 MeV; therefore, the influence of these gamma-rays on the systematic uncertainty is small [53]. When 3 MeV gamma-rays are simulated, the NCQE-gamma event rate changes less than 1%. Therefore, the uncertainty of gamma-rays below 3 MeV is set to 1%.

- Multi-hole states

Approximately 40% of NCQE events emit multiple nucleons. However, the de-excitation gamma-ray emission rate from multi holes is not well understood. Therefore, in multi-hole state, it is assumed that gamma-rays above 3 MeV are not emitted. When errors are maximally shifted, the NCQE-gamma event rate changes by 9%. Therefore, the uncertainty of multi-holes states is set to 9%.

- Total NCQE gamma uncertainty

In total, $\pm 10\%$ uncertainty is assigned to the production rate of the prompt nuclear de-excitation gamma- rays following neutrino interactions.

5.3 Secondary gamma

The uncertainty from secondary gamma-rays mainly stems from neutron-water interactions, which are not well understood. The NMTC and MICAP simulators provide the data [55]. This uncertainty is 12%.

5.4 Super-Kamiokande

The SJ displays some response uncertainties. Although it is regularly calibrated and the detector response is well understood, some uncertainties remain. As discussed in Section 4, NCQE events are selected at various threshold cuts. The SK detector response uncertainty is 2.2%, which is calculate using SK calibration data.

5.5 Oscillation parameters

In this thesis, the neutrino oscillation parameters are set to fixed value presented in Table 1. The number and type of NCQE interactions via neutrino oscillation do not change, as NCQE interactions do not depend on the neutrino type. However, the number of background events changes due to neutrino oscillation, because background events have charged current events that depend on neutrino oscillation. The uncertainty of CC events due to the neutrino oscillation parameters is limited to 6% in various experiments. In addition, only 4% of the de-excitation gamma-ray events result from CC events.Therefore, the uncertainty caused by neutrino oscillation is set to 0.24%. Table 10 summarizes each uncertainty.

Table 10: Summary of uncertainties caused by oscillation parameters.

Interaction	$+\Delta m^2_{23}$	$-\Delta m^2_{23}$	$+\sin^2\theta_{23}$
CC error	+3.5%	+0.5%	+9.2%

5.6 Beam-unrelated event

In this subsection, the uncertainty of beam-unrelated events is estimated. A very narrow time window, -500 μs to 5 μs, which is correlated to the beam timing, is analyzed in the T2K experiment data. However, background events such as cosmic neutrinos are often observed. Therefore, 505 μs is multiplied by the number of spills in T2K-Run1-4. The total time of T2K-Run1-4 is 23 hours.

5.7 Uncertainty result

Table 11 lists the systematic uncertainty of each interaction and factor. De-excited gamma-ray events caused by true NCQE interactions constitute is 72% of the total events. Therefore, the largest uncertainty stems from secondary gamma-rays.

Table 11: Summary of systematic uncertainties.

Interaction	NCQE	NCother	CC	beam-unrelated
Event ratio	71.9%	23.1%	3%	2%
Flux	11%	10%	12%	-
Cross-section	-	18%	24%	-
Primary γ	10%	3%	6%	-
Secondary γ	13%	13%	7.6%	-
SK detector	2.1%	2.1%	2.1%	-
Oscillation parameters	-	-	6%	-
Total	20%	25%	30%	0.8%

6 NCQE cross-section

In this section, the final NCQE cross-section result is presented and averaged for the T2K beam flux energy.

6.1 Theoretical NCQE cross-section by the T2K neutrino beam

The average of the theoretical NCQE cross-section for the T2K beam flux energy is calculated by following equation;

$$< \sigma^{theory}_{\nu,NCQE} >= \sum_{E_i} \sigma^{theory}(E_i)\Phi_{flux}(E_i) \tag{28}$$

where, $\sigma(E_i)$ is the NCQE cross-section for each energy described in Section 3.2.1 and $\Phi_{flux}(E_i)$ is the T2K beam flux described in Section 3.1. The result is $< \sigma^{theory}_{\nu,NCQE} >= 2.01 \times 10^{-38} cm^2$. Using this averaged NCQE cross-section, the expected number of interactions in T2K Run1-4 comprises 100.2 events.

6.2 Measurement of NCQE cross-section

The observed NCQE cross-section,$< \sigma^{observation}_{\nu,NCQE} >$, is measured by scaling the theoretical cross section, $< \sigma^{theory}_{\nu,NCQE} >$, and is calculated as follows;

$$< \sigma^{observation}_{\nu,NCQE} >= \frac{N^{observation} - N^{expect}_{background}}{N^{expect}_{total} - N^{expect}_{background}} \times < \sigma^{theory}_{\nu,NCQE} > \tag{29}$$

where, $N^{observation}$ is the number of observed NCQE events (102), N^{expect}_{total} is the number of expected NCQE events (100.2), and $N^{expect}_{background}$ is the number of expected background events (28.0); here the numbers in parentheses are the results from T2K Run1-4. When these numbers are substituted into equation 30

$$< \sigma^{observation}_{\nu,NCQE} >= \frac{102 - 28.0}{100.2 - 28.0} \times 2.01 \times 10^{-38}[cm^2] = 2.07 \times 10^{-38}[cm^2] \tag{30}$$

6.3 Uncertainty of NCQE cross-section

The total uncertainty is calculated using a Toy MC simulation [50], which uses generated random numbers based on a Gaussian distribution. It is obtained by shifting the error, which includes all of the uncertainties described in Section 5. Figure 49 illustrates the calculation method. In this method, the change in the number of events for every systematic uncertainty in each interaction, NCQE, NC other and CCQE, is calculated. The statistical uncertainty is also added, and the total uncertainty is obtained. Figure 50 presents the NCQE cross-section distribution, including systematic and statistical uncertainty.

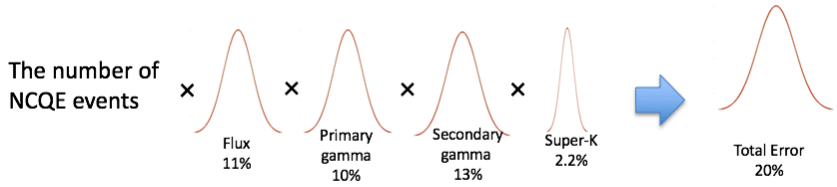

Figure 49: Calculation method of total systematic uncertainty.

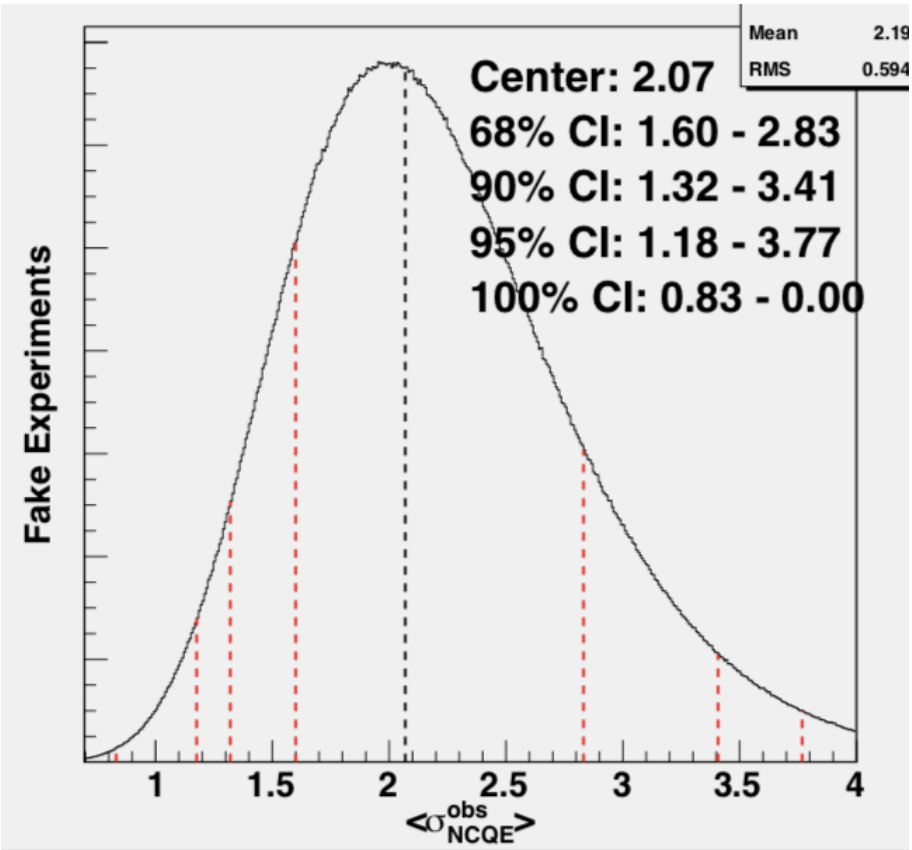

Figure 50: NCQE cross-section distribution for the T2K RUN1-4 observation, performed using a Toy MC simulation.

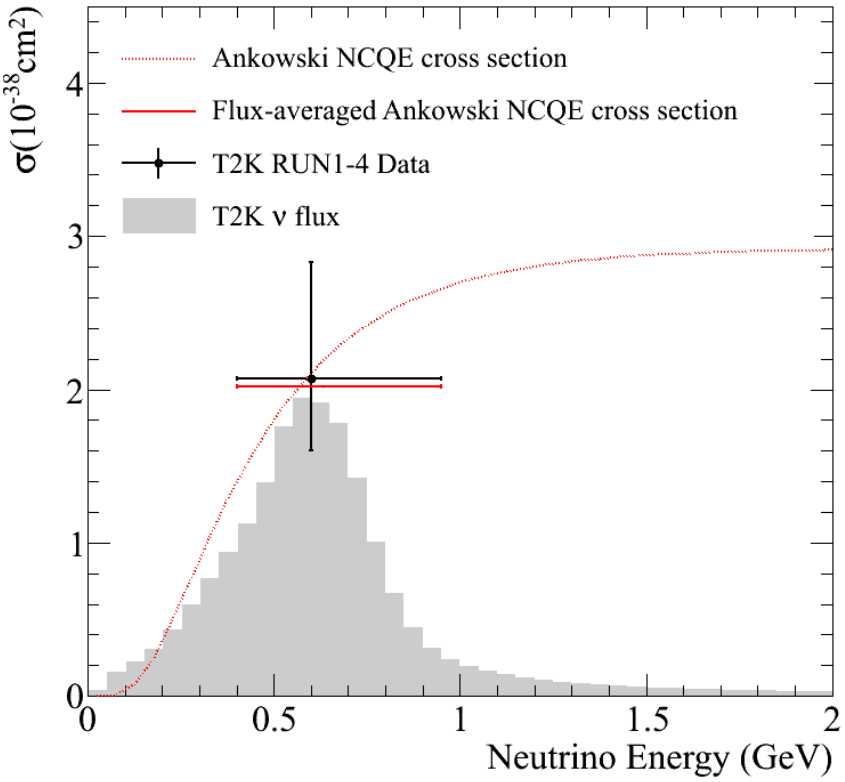

Figure 51: The T2K Run1-4 data and theoretical flux-avaraged NCQE cross-section by T2K. The black point and the error-line are the measurement results in the analysis [29]. The red line is a theoretical cross-section. Both error-line intervals are displayed at 68% confidence levels. The gray histogram illustrates the T2K neutrino flux in the SK

6.4 Results

The measurement of the T2K beam flux averaged neutrino-water NCQE cross-section is as follows:

$$2.01 \times 10^{38} cm^2 \pm 0.27(stat,) \pm^{0.69}_{0.39} (Sys.) \tag{31}$$

Figure 51 presents a comparison between the theoretical estimates and the analytical results. The measured NCQE cross-section is consistent with the theory at 68% C.L.

7 Neutron tagging via NCQE interaction

As described in Section 5.3, the gamma emission rate from secondary neutrons in the current NCQE interaction simulation has a large uncertainty. This uncertainty has an impact not only on the secondary gamma emission rate in the measurement of the NCQE cross section but also on the background evaluation for the SRN search, as described in Section 1.4. This section discusses, neutron detection from 102 NCQE events in the T2K experiment, which is analyzed in Section 6.

7.1 Neutron capture in water

First, neutron reactions in water are addressed. In an NCQE interaction, nucleons (proton or neutron) are emitted. Protons quickly lose energy by ionization loss. By contrast, neutrons do not cause electromagnetic interactions because they have no charge. Therefore, neutrons collide with more nuclei than protons do. Secondary neutrons are then generated, which is discussed in Section 3.3.1, and briefly explained below. Figure 36 illustrates the energy of the nucleon. Neutron lose energy by elastic scattering; next, they are thermalized ($\sim$0.025 eV). Then, nearly all of the neutrons are absorbed by a hydrogen nucleus because the neutron capture cross section of a hydrogen nucleus (330 millibarns) is larger than that of an oxygen nucleus (0.19 millibarns). The neutron capture hydrogen then releases 2.2 MeV gamma rays as follows:

$$n + p \rightarrow d + \gamma(2.2MeV) \tag{32}$$

The lifetime of neutron capture is measured as 204.8 μs [56], and 2.2 MeV gamma-rays are the targets for neutron tagging analysis in this thesis.

7.2 Neutron tagging algorithm

In this subsection, a neutron tagging algorithm in the SK is described [58]. In this thesis, the gamma-rays of neutron capture are searched by multivariate analysis using neural networks, which are part of machine learning. In brief, the pattern recognition learning of signals is performed by machine learning using a neutron capture simulation. Then, actual NCQE signal data are also analyzed by pattern recognition using the learned information.

The identification of 2.2 MeV gamma-rays which are neutron tagging gamma-rays, is split into two steps.

- Step 1: N_{10} selection

First, the peaks in the timing distribution are searched to select the initial 2.2 MeV candidates.

- Step 2 : Neutron distinction

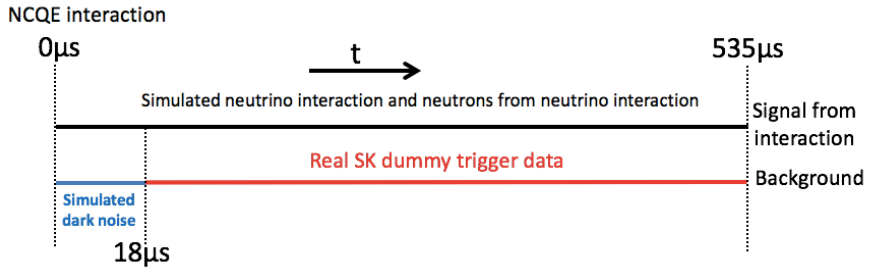

Figure 52: Construction of neutron simulation. After 18μs, the T2K dummy trigger data are added.

Second, a set of 22 reconstruction variables for each gamma candidate is calculated and inputted to the neural network. The final selection of 2.2 MeV gamma-rays is based on the output of this neural network.

The main backgrounds in this energy range includes radioactive decay from rocks outside the detector, radon contamination in the water, PMT dark noise and others.

7.2.1 Neutron simulation via NCQE interaction

First, a simulation only for machine learning is created. The differences between the neutron capture gamma signal patterns and background signal patterns are learned by this simulation. This simulation is simulated 500 μs after NCQE events. In addition, the 2.2-MeV gamma rays emitted when neutrons are captured are simulated. However, background simulation uses a special method, as described below.

n the general SK simulation, all PMTs are evenly provided an averaged background event rate resulting from a random background consisting of PMT dark noise and radiation. In common NCQE events analysis., this method does not pose a problem. However, the random background noise method presents a problem in the neutron tagging simulation because a background with random noise cannot reproduce the actual background of the SK. Therefore, real data, which consist of T2K dummy trigger data, are used as background data. Each dummy event consists of 1 ms of data. The dummy trigger events are selected by allowing only a narrow range of total hits (50,000 $<$ Number of hits $<$55,000 in 1 ms) to eliminate events contaminated with cosmic ray muons and other miscellaneous phenomena. Since each event requires only 500 μs of data because the simulation time is 500 μs, each dummy event is shared between two events. The total frequency of the background is identical to the background generated in the simulation. This dummy trigger data are added after 18 μs after the main events in the simulation, which involves no simulated background 18 μs after the main events. Figure 52 illustrates this method.

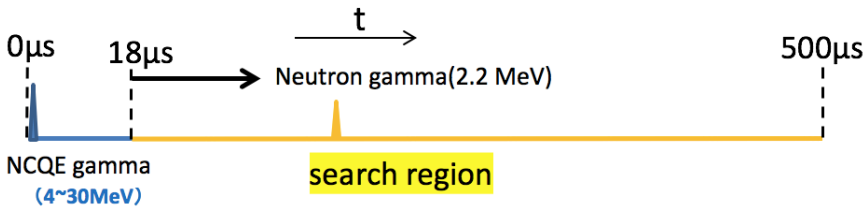

Figure 53: Neutron search region. Only the yellow region is searched.

7.2.2 First selection of neutron capture gamma (N_{10} selection)

All PMT hits are the TOF subtracted from the NCQE event vertex. The first selection is made for the NCQE events in the actual data and the simulation data. Then, N_{10}, which is the number of PMT hits in a 10 ns window, is calculated from the 18 μs to the 500 μs region following the NCQE interaction. When N_{10} is greater than 7 and less than 50, it is selected. Figure 53 presents the N_{10} selection region. The region up to 18 μs is not analyzed because it has a large background effect caused by the after pulse, which is the background signal of PMTs due to residual gas. However, if the number of PMT hits $\pm$100 ns (N_{200}) around N_{10} selection events is greater than 200, the events are rejected. The reason for this is to remove contamination, such as cosmic ray muon events, radiation background, and spallation. Incidentally, a 1 MeV gamma-ray hits an average of six PMTs in the SK. The efficiency of the remaining true neutrons from this selection is 33%, and the background event rate for a single NCQE event is 4.4 events.

7.2.3 Reconstructed variables for neural network

Following the N_{10} selection, 22 reconstruction variables are calculated, which can distinguish 2.2 MeV gamma rays from the background signal. The variables are then inputted to the neural network. The 22 variables are summarized in Table 12 and illustrated in Figure 54, 55, 56 and 57.

7.2.4 Training via Neural Network

First candidate events (discussed in section 7.2.2) are separated into 2.2 MeV gamma-rays and background using a neural network. A neural network is a tool based on machine learning that is used primarily for pattern recognition in fields such as image analysis, marketing and signal background classification in particle physics. In this thesis, the Toolkit for Multivariate Analysis (TMVA) application that includes the ROOT analysis framework is used for neural network analysis. A Multi-Layer Perceptron (MLP) is used in multivariate analysis [57].

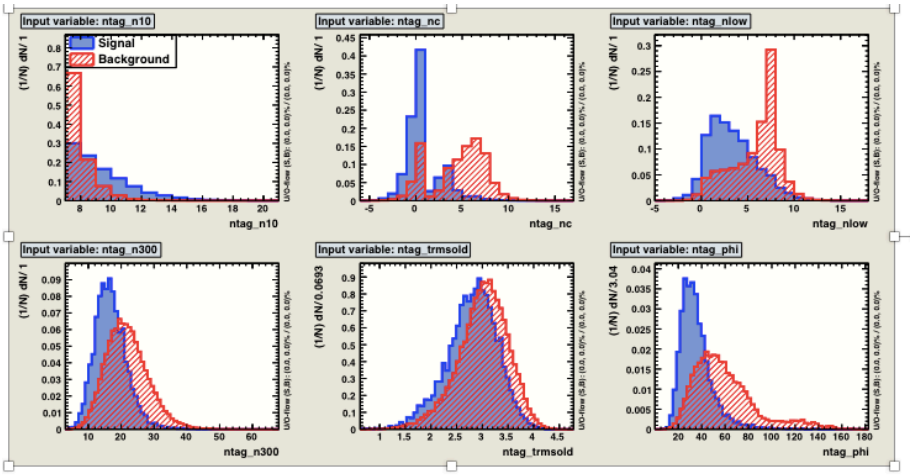

Figure 54: Difference between the signal and background with reconstructed variables. Red represents neutron capture gamma-rays, and blue represents the background signal.

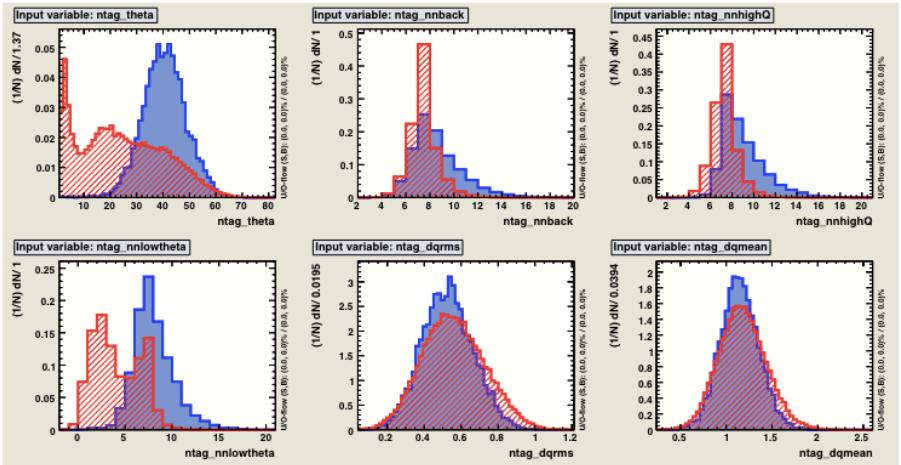

Figure 55: Difference between the signal and background with reconstructed variables. Red represents neutron capture gamma-rays, and blue represents the background signal.

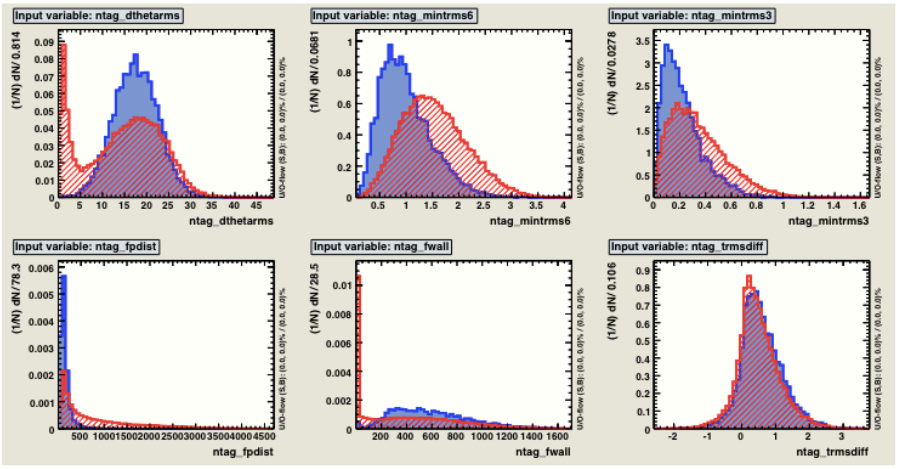

Figure 56: Difference between the signal and background with reconstructed variables. Red represents neutron capture gamma-rays, and blue represents the background signal.

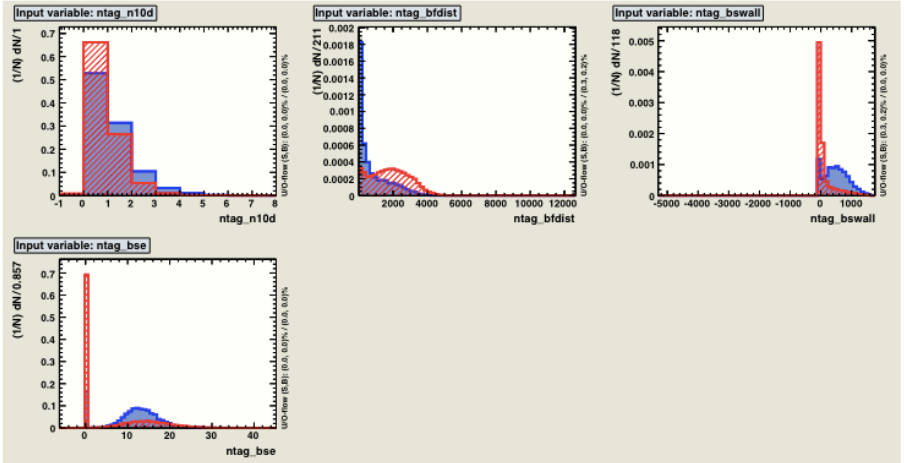

Figure 57: Difference between the signal and background with reconstructed variables. Red represents neutron capture gamma-rays, and blue represents the background signal.

Table 12: Summary of 22 reconstruction variables.

Variable Name	Description
N_{10}	Hit counts of 10ns window
N_{300}	Hit counts within $\pm$ 150ns at N_{10}
N_{10d}	Number of hits in 10 ns minT_{rms} vertex − N_{10}
N_c	Position relation of hits PMT
N_{low}	Number of low probability hitting PMT
N_{back}	Number of hits in backward direction in N_{10}
N_{highQ}	Check HighQ events in N_{10}
$N_{low\theta}$	Check $\Theta < 20^\circ$ events in N_{10}
T_{rms}	Minimum of N_{10} Timing RMS
T_{rmsd}	Trmsold - Trms
Q_{rms}	N_{10} Qrms
Q_{mean}	N_{10} Qmean
Q_{bonsai}	bonsai reconstruction energy
V^{N10d}	Difference between parent particle and N_{10} vertex
V_{fwall}	Reconstructed dwall using Neut fitv
V_{bonsai}	Neutron Bonsai vertex
V_{bswall}	distance of bonsai vertex to wall
ϕ	root mean square of hits at ϕ
θ	Theta mean of hits
θ_{rms}	θ RMS
Min$T_{rms}6$	Minimum T-rms of clusters of 6 hits out of N_{10}.
Min$T_{rms}3$	Minimum T-rms of clusters of 3 hits out of N_{10}.

In the analysis, 1.04 $\times 10^6$ events were generated in the NCQE interaction simulation, where ν_μ is 1.00 $\times 10^6$, ν_e is 0.02 $\times 10^6$ and $\overline{\nu}_\mu$ is 0.02 $\times 10^6$ events whose ratio is the NCQE interaction rate to the T2K beam. 75% of the simulation events were used for neural network training, and the remaining 25% were used to verify the training result without the actual neutron information.

7.2.5 Neural Network results

The output of the neural network has a value of approximately $0 \sim 1$. This value is referred to as the MLP value. In the training, if the MLP value is large, it is likely to represent a neutron. However, if it is closer to 0, it is likely to represent the background. Figure 58 presents the training (Train $\times\times$) and test (Test $\times\times$) result. Real information on 2.2 MeV gamma rays and background is used in training but

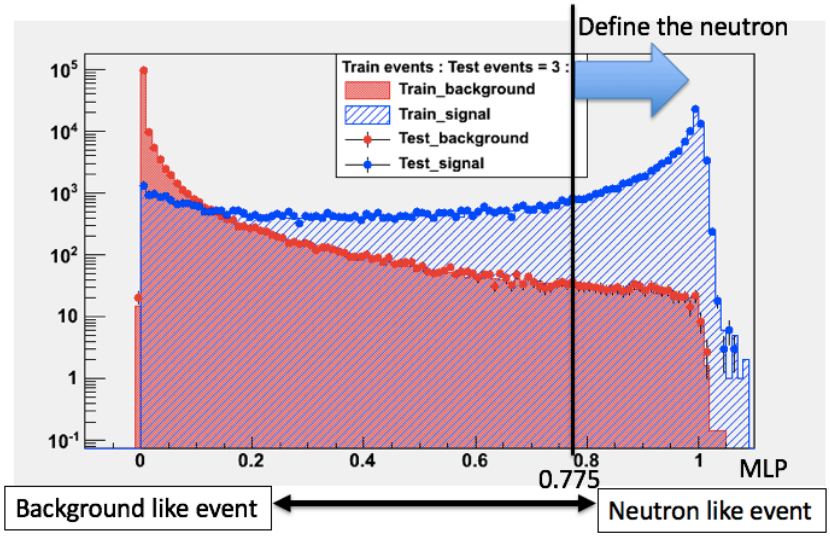

Figure 58: Training and test results. Red represents training true background signal, and blue represents training the true 2.2 MeV gamma signal. Red dots represent the test background signal, and blue dots represent the true 2.2 MeV gamma signal. In this analysis, MLP $>$ 0.775; to the right of the black line, 2.2 MeV gamma signals are defined.

not in testing.In testing, the MLP value is calculated using the distinction condition produced in training. Figure 58 illustrates the successful identification.

Thereafter, the MLP threshold is defined. In this analysis, it is set to less than 2% of the background rate per NCQE event. The background means that a non 2.2 MeV gamma signal is judged to be a 2.2 MeV gamma signal. An MLP $>$ value above 0.775 implies a neutron. The right side of the dotted line in Figure 58 is considered a neutron capture 2.2 MeV gamma-ray, and the left side of the line is considered a background event.

7.2.6 Neutron tagging efficiency

Neutron capture efficiency is calculated as the ratio of the number of captured neutron events to the number of generated true neutron events in the tested simulation. Figure 59 presents a flowchart and the number of events at each step. The number of neutrons generated by the tested simulation is 126,756. By contrast, the number of events judged to be neutrons when MLP $>$ 0.775 is 30,856. Therefore, the trapping efficiency is calculated as follows: $30,856/126,756 = 24.3\%$.

This efficiency is compared using calibration data by AmBe. The systematic error of the neutron capture efficiency is estimated at approximately 10%, as the capture efficiency of AmBe is 26.9%.

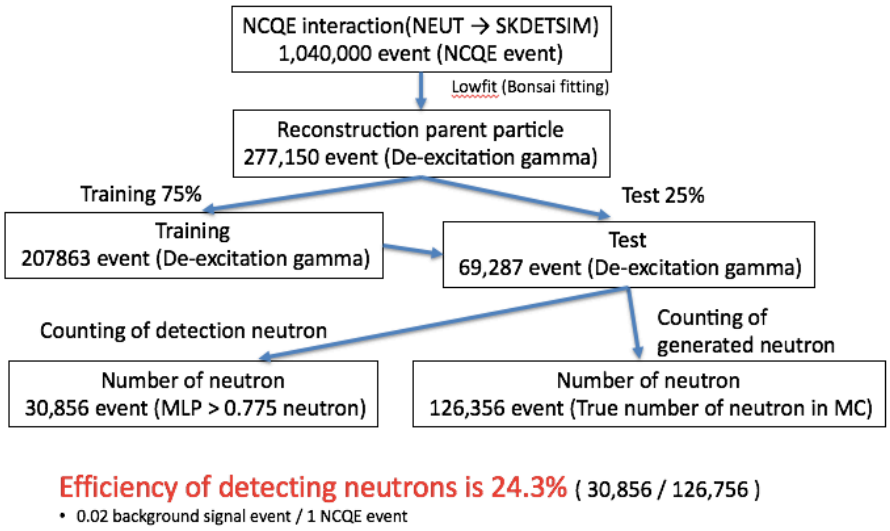

Figure 59: Flowchart of efficiency calculation. 126,356 neutrons are captured in the MC simulation, and 30,856 neutrons are determined by MLP > 0.775. Therefore, the neutron capture efficiency is 30,856/126,356 = 24.3%.

7.3 Neutron tagging in NCQE data

Using the neural network results, the NCQE data are analyzed in terms of the neutron tagging 2.2 MeV gamma-rays. The T2K triggered SK data are saved all PMT hits date of each spill $\pm$ 500 μs. Therefore, the NCQE data are analyzed from 18 μs to 500 μs, as it is in the simulation.

7.3.1 Results

The NCQE interaction data consisting of 102 events were analyzed by the neural network, are the first choice neutron candidates were obtained from 483 events. Among them, 32 events were determined to be neutron events with MLP > 0.775. However, 2.04 events, which were calculated from 2% of 102 events, were expected to be contamination. There were 23 single neutron events within one NCQE event, 3 two-neutrons events, and three-neutrons event. Figure 60 presents the results of neutron tagging. In addition, Figure 61 illustrates the multiplicity of the neutron for a single event resulting from the data and simulation. In this analysis, the neutron tagging efficiency is 24.3%. Therefore, in an actual interaction in the SK, 4.1 times more neutrons are emitted as in the observed values.

7.3.2 Number of secondary neutron

An average of 1.77 events from a single NCQE event are observed in the current simulation between 18 μs to 500 μs. By contrast, an average of 1.21 $\pm$ 0.27 events in

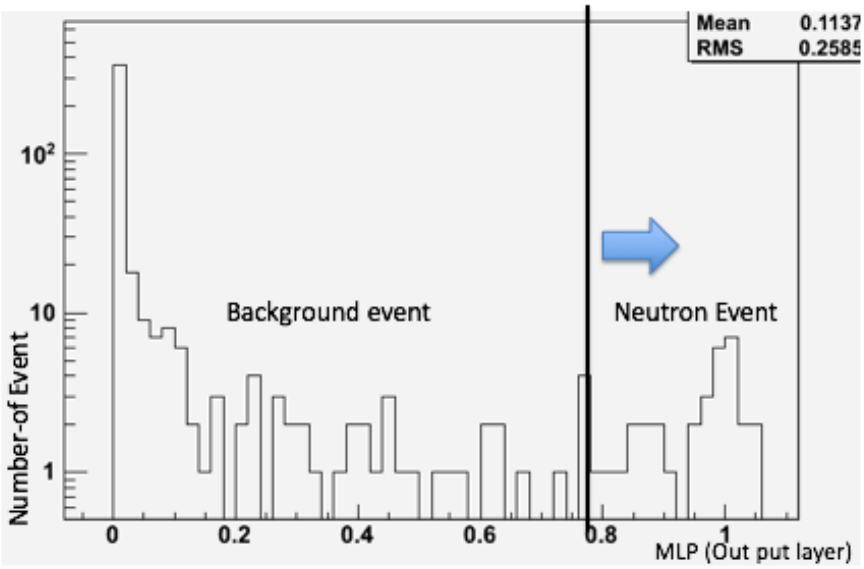

Figure 60: Training results using an MC simulation applied to data. The 32 events are MLP > 0.775.

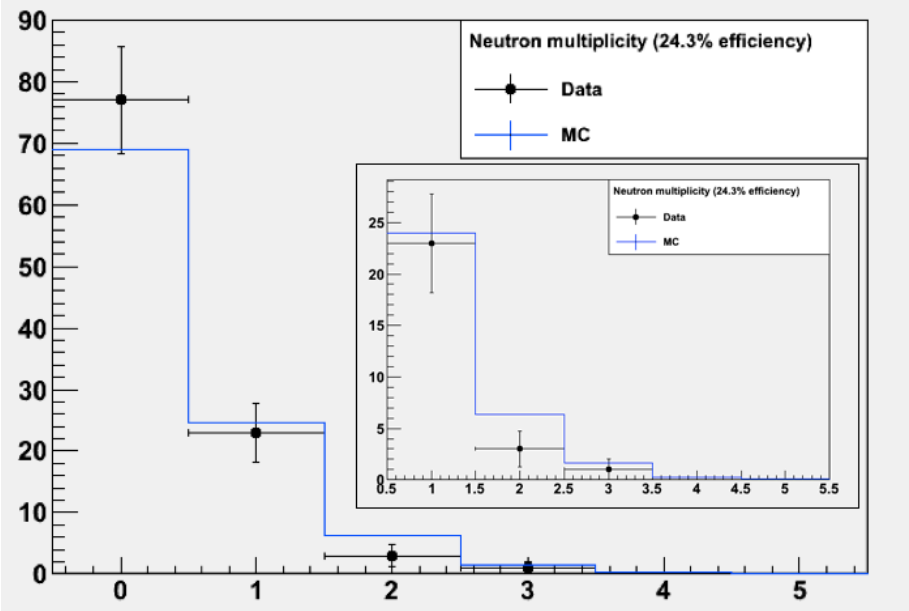

Figure 61: Neutron multiplicity for each NCQE event. The dots represent the data, and blue histogram represent the expected multiplicity by MC simulation.

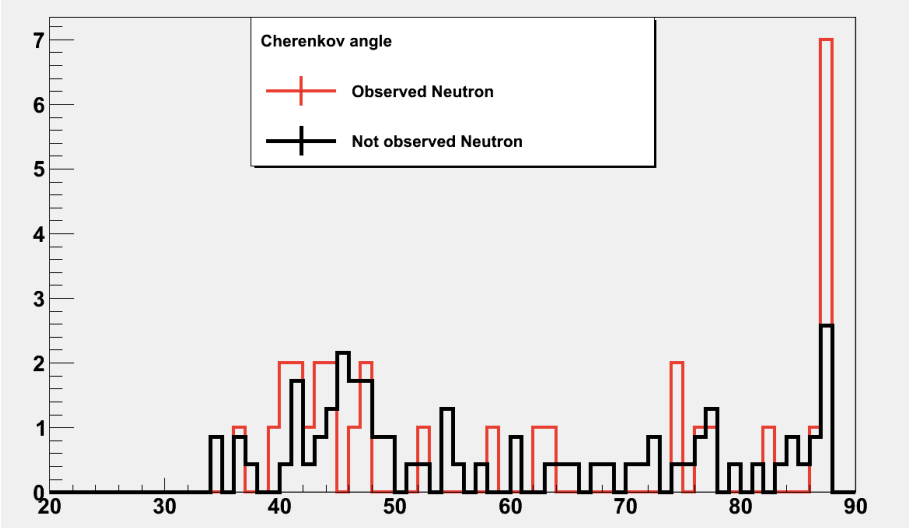

Figure 62: Cherenkov angle distribution with and without neutron NCQE events. Red represents an observed neutron, and black represents a neutron that is not observed. Black is normalized by the total number of red events.

a single NCQE event are observed in the actual data. This result is suggests that, in the current simulation, many more neutrons are generated than in an actual interaction. This is one of the causes of the NCQE systematic error, which is discussed in Section 5.3.

7.3.3 NCQE Cherenkov angle distribution

The Cherenkov angle results are presented in Figure 44. There are two peaks at approximately 42° and 90°. The peak near 42° is due to a single gamma ray, and peak near 90° suggests that multiple gamma rays emitted. However, evidence for the latter has not been demonstrated by actual data analysis.

Figure 62 illustrates the Cherenkov angle distribution with and without neutron events. The result suggests that with neutron NCQE events are more likely to be distributed near 90°.

8 Conclusion

In this thesis, measurement of NCQE interactions in the T2K experiment in Run1-4 and neutron capture gamma-rays via this interaction were presented. The main motivation of this measurement is to estimate the atmospheric neutrino background for future SRN search experiments, since SRN signal are similar to NCQE signals.

De-excitation gamma-rays due to NCQE interactions are primarily in the vicinity of 6 MeV. Their cross-section is measured by comparing the number of expected and observed events. The average cross-section at the T2K flux is $< \sigma^{Theory}_{\nu,NCQE} >= 2.01 \times 10^{-38} cm^2$. The number of de-excitation gamma-ray events in the MC simulation in the T2K Run1-4 (from June 2010 $\sim$ May 2013) is 100.2; this includes 28.0 background events and 72.2 NCQE events. The T2K data contain 102 NCQE like events; ss a result, the NCQE cross-section is demonstrated to be

$$< \sigma^{obs}_{NCQE}, T2KRun1 \sim 4 >= 2.07 \pm 0.27(stat) \pm^{0.69}_{0.39} (Sys.) \times 10^{-38} \quad (33)$$

Thereafter, 2.2 MeV gamma-rays by neutron capture were searched for among 102 NCQE events. Multivariate analysis via a neural network was used for the analysis. The results demonstrate that 32 neutron events were found. The neutron capture efficiency was thus 24.3%, and the number of background events was estimated to be 2.04 in this analysis. The with neutron events were more likely to have Cherenkov angle distributions at approximately 90°. In addition, the estimated number of neutrons in the current simulation was 1.77 in an NCQE event. However, 1.21 ± 0.27 events were observed in the data. This result suggests that the number of secondary neutrons generated in the current simulation is larger than that in the real data.

References

[1] B. Pontecorvo, "Inverse beta process and nonconservation of lepton charge", Sov. Phys. JETP 7, 172-173(1958)

[2] B. Pontecorvo, "Neutrino experiments and the problem of conservation of leptonic", Sov. Phys. JETP 26, 984-988(1968)

[3] Ziro Maki, Masami Nakagawa, and Shoichi Sakata, "Remarks on the Unified Model of Elementary Particles", Prog. of Theo. Phys. 28, No. 5(1962)

[4] M. Tanabashi et al. (Particle Data Group) Phys. Rev. D 98, 030001 (August 2018)

[5] F. Reines and Clyde L. Cowan Jr., "Free Antineutrino Absrobtion Cross Section. I. Measurement of the Free Antineutrino Absorption Cross Section by Protons", Phys. Rev. 113, 273(1959)

[6] F. J. Hasert, et al., "Observation of neutrino-like interactions without muon or elec- tron in the GARMELLE neutrino experiment", Phys. Lett. 46B, 138(1973)

[7] S. Ando, K. Sato and T. Tonani, "Detectability of the supernova relic neutrinos and neutrino oscillation", Astropart. Phys. 18, 307-318(2003)

[8] K. Bays, T. Ilda, et al. (Super-Kamikande collaboration), "Supernova relic neutrino search at Super-Kamiokande", Phys. Rev. D 85, 052007(2012)

[9] H. Zhang, et al. (Super-Kamikande collaboration), "Supernova Relic Neutrino Search with Neutron Tagging at Super-Kamiokande-IV", Astropart. Phys. 60, 41-46(2015)

[10] J. Kameda, "Observation of de-excitation gamma rays from nuclei in 1kton detector in K2K experiment", Nucl. Phys. B(Proc. Suppl.) 159, 44-49(2006)

[11] H.-Th. Janka, et al., "Theory of core-collapse supernovae", Phys. Repo. 442, 38- 74(2007)

[12] K. Abe, et al. et al. (T2K collaboration) "Measurement of the neutrino-oxygen neutral-current interaction cross section by observing nuclear deexcitation γ rays", Phys. Rev. D 90, 072012 (2014)

[13] K. Abe, et al. (T2K collaboration), "The T2K Experiment", Nucl. Instr. Meth. A 659, 106-135(2011)

[14] K. Abe, et al. (T2K collaboration), "Indication of Electron Neutrino Appearance from an Accelerator-produced Off-axis Muon Neutrino Beam", Phys. Rev. Lett. 107, 041801(2011)

[15] A. K. Ichikawa, “Design concept of the magnetic horn system for the T2K neutrino beam”, Nucl. Instr. Meth. A 690, 27-33(2012)

[16] K. Matsuoka, “Measurement of the Neutrino Beam with the Muon Monitor and the First Result of the T2K Long-Baseline Neutrino Oscillation Experiment”, PhD thesis, Kyoto Univ., (2011)

[17] K. Abe, et al. (T2K collaboration), “Measurements of the T2K neutrino beam properties using the INGRID on-axis near detector”, Nucl. Instr. Meth. A 694, 211- 223(2012)

[18] K. Abe, et al. (T2K collaboration), “The T2K Experiment”, Nucl. Instr. Meth. A 659, 106-135(2011)

[19] S. Fukuda, et al. (Super-Kamikande collaboration), “The Super-Kamiokande detector”, Nucl. Instr. Meth. A 501, 418-462(2003)

[20] A. Suzuki, et al., “Improvement of 20 in. diameter photomultiplier tubes”,

[21] Nucl. Instr. Meth. A 329, 299-313(1993) S. Yamada et al., “Commissioning of the New Electronics and Online System for the Super-Kamiokande Experiment”, IEEE Transactions on Nucl. Scie, 57 428(2010)

[22] Takaaki Mori, “Development of A Gadolinium-doped Water Cherenkov Detector for The Observation of Supernova Relic Neutrinos”, PhD Thesis, The University of Okayama, (2015)

[23] G. Battistoni, F. Broggi, M. Brugger, M. Campanella, M. Carboni et al., “Applica- tions of FLUKA Monte Carlo code for nuclear and accelerator physics”, Nucl. Instr. Meth. B 269, 2850(2011)

[24] N. Abgrall et al.(NA61/SHINE Collaboration), “Measurement of Cross Sections and Charged Pion Spectra in proton-carbon Interactions at 31GeV/c”, Phys. Rev. C 84, 034604(2011)

[25] N. Abgrall et al.(NA61/SHINE Collaboration), “Measurement of Production Proper- ties of Positively Charged Kaons in Proton-Carbon Interactions at 31 GeV/c”, Phys. Rev. C 85, 035210(2012)

[26] R. Brun, F. Carminati, and S. Giani, “GEANT Detector Description and Simulation tool”, CERN-W5013 (1994)

[27] A. Abe et al.(T2K Collaboration), “T2K neutrino flux prediction”, Phys. Rev. D 87, 019902(2013)

[28] Y. Hayato, Nucl. Phys. Proc. Suppl. 112 171(2002)

[29] Artur M. Ankowski and Omar Benhar, "Analysis of γ-Ray Production in Neutral- Current Neutrino-Oxygen Interactions at Energies above 200 MeV", Phys. Rev. Lett. 108, 052505(2012)

[30] O. Benhar, N. Farina, H. Nakamura, M. Sakuda, and R. Seki, "Electron- and neutrino-nucleus scattering in the impulse approximation regime" Phys. Rev. D 72, 053005 (2005).

[31] O. Benhar and D. Meloni, "Total neutrino and antineutrino nuclear cross sections around 1 GeV" Nucl. Phys. A 789, 379 (2007).

[32] M. K. Jones et al., "GEp /GMp Ratio by Polarization Transfer in $\vec{e}\mathrm{p} \rightarrow \mathrm{e}\vec{p}$", Phys. Rev. Lett. 84, 1398(2000)

[33] R. Bradford, A. Bodek, H. Budd, and J. Arrington, "A New Parameterization of the Nucleon Elastic Form Factors", Nucl. Phys. Proc. Suppl. 159, 127-132(2006)

[34] Omar Benhar et al., "Spectral function of finite nuclei and scattering of GeV elec- trons", Nucl. Phys. A 579, 493-517(1994)

[35] M. Bernheim et al., "The influence of bound state and optical potentials on 1p momentum distributions obtained from 12C and 16O$(e, e'p)$ reactions", Nucl. Phys. A 375 (1982) 381-404

[36] D. Rohe et al.(E97-006 Collaboration), "Correlated Strength in the Nuclear Spectral Function", Phys. Rev. Lett. 93, 182501

[37] H. Ejiri, "Nuclear deexcitations of nucleon holes associated with nucleon decays in nuclei", Phys. Rev. C 48, 48(1993)

[38] M. Leuschner et al., "Quasielastic proton knockout from 16O", Phys. Rev. C 49, 955(1994)

[39] F. Ajzenberg-Selove. "Energy Level of Light Nuclei", Nucl. Phys. A 523, 1(1991)

[40] K. Kobayashi, et al., "De-excitation γ-rays from the s-hole state in 15N associated with proton decay in 16O", arXiv:nucl-ex/0604006 [nucl-ex].

[41] M. Yosoi, et al., "Cluster fragmentations of deep(1s)-hole states in light nuclei", Nucl. Phys. A 738, 451(2004)

[42] M. Yosoi, et al., "Structures and decay of deep-hole states in light nuclei populated by the (p,2p) reactions", Phys. Atom. Nucl. 67, 1810(2004)

[43] R. Brun, F. Carminati, and S. Giani, "GEANT Detector Description and Simulation tool", CERN-W5013 (1994)

[44] C. Zeitnitz and T. Gabriel, "The GEANT-CALOR interface and benchmark calculations of ZEUS test calorimeters", Nucl. Instr. Meth. A 349, 106-111(1994)

[45] T. A. Gabriel, Proceedings of the Workshop on Simulating Accelerator Radiation Environments, "The CALOR93 Code system", 1994

[46] Hugo W,Bertini, "Intranuclear-Cascade Calculation of the Secondary Nucleon Spectra from Nucleon-Nucleus Interactions in the Energy Range 340 to 2900 MeV and Comparisons with Experiment", Phys. Rev. 188, 1711 (1969)

[47] K. Matsuoka, "Measurement of the Neutrino Beam with the Muon Monitor and the First Result of the T2K Long-Baseline Neutrino Oscillation Experiment", PhD thesis, Kyoto Univ., 2011

[48] Michael Smy for the Super-Kamiokande Collaboration, "Low Energy Event Reconstruction and Selection in super-Kamiokande-III", in Proceedings of 30TH International Cosmic Ray Conference, Mexico city, Mexico, 2008, Vol.5 (HE part2), pages 1279-1282

[49] A. Abe et al.(SK Collaboration), "Solar neutrino results in Super-Kamiokande-III", Phys. Rev. D 83, 052010(2011)

[50] K. Huang, "Measurement of the Neutrino-Oxygen Neutral Current Quasi-elastic Interaction Cross-section by Observing Nuclear De-excitation gamma-rays in the T2K Experiment", PhD thesis, Kyoto Univ., (2015)

[51] K. Abe, et al. (T2K Collaboration), "Measurements of neutrino oscillation in appearance and disappearance channels by the T2K experiment with 6.6 $\times$ 1020 protons on target", Phys. Rev. D 91, 072010(2015)

[52] M. Leuschner et al., "Quasielastic proton knockout from 16O", Phys. Rev. C 49, 955(1994)

[53] Yuri Kamyshkov and Edwin Kolbe, "Signatures of nucleon disappearance in large underground detectors", Phys. Rev. D 67, 076007(2003)

[54] K. Kobayashi, et al., "De-excitation γ-rays from the s-hole state in 15N associated with proton decay in 16O", arXiv:nucl-ex/0604006 [nucl-ex]

[55] T. A. Gabriel, Proceedings of the Workshop on Simulating Accelerator Radiation Environments, "The CALOR93 Code system", (1994)

[56] D. Cokinos and E. Melkonian. Measurement of the 2200m/sec neutron-proton capture cross section. Phys. Rev. C, 15:1636, (1977)

[57] A. Hoecker, P. Speckmayer, J. Stelzer, J. Therhaag, E. von Toerne, H. Voss(Cern ROOT), "TMVA — ROOT a Data analysis Framework, Toolkit for Multivariate Data Analysis with ROOT Users Guide" ,arXiv:physics/0703039

[58] H. Zhang et. al (Super Kamiokande Collaboration) H. Watanabe. First study of neutron tagging with a water cherenkov detector. Astropart. Phys., 31:320 – 328, (2009)